SAE INTERNATIONAL

ARTICLE INFO
Article ID: 10-11-01-0005
© 2027 Clemens Deubel, Johannes Meinck, Tobias Schramm, Günther Prokop
doi:10.4271/10-11-01-0005

Enhanced Suspension Friction Modeling for Vehicle Vertical Dynamics Simulation

Clemens Deubel,[1] Johannes Meinck,[2] Tobias Schramm,[2] and Günther Prokop[2]

[1]Technische Universität Dresden, Institute of Automobile Engineering, Germany
[2]Technische Universität Dresden, Germany

Abstract

Accurate suspension modeling is essential for virtual vehicle development. While stiffness and damping characteristics are commonly represented in considerable detail, the influence of suspension friction modeling on vehicle vertical dynamics has not yet been systematically assessed. This study introduces and validates a side force–dependent friction modeling framework for MacPherson suspensions within a full-vehicle simulation environment. Since shock absorber friction strongly depends on the acting side force, a methodology is developed to determine the instantaneous side force from the current suspension kinematic and kinetic state, accounting for suspension deflection as well as tire forces and moments. Three friction model variants—a nominal model, a quasi-static side force–dependent model, and a dynamic side force–dependent model—are evaluated under cornering, longitudinal maneuvers, and uneven road excitation. Their influence on vertical, roll, and pitch dynamics is assessed using objective discomfort indicators. The results show that side force–dependent friction modeling substantially improves the physical representation of suspension friction and its influence on vehicle dynamics. However, the additional complexity of dynamic friction modeling provides only limited benefit, as friction effects become less relevant once hydraulic damping dominates. The quasi-static formulation therefore offers the most favorable balance between modeling effort and accuracy. The proposed approach provides a physically motivated and practically applicable enhancement of MacPherson suspension friction modeling and demonstrates that accurate friction representation is particularly important under low-speed and smooth road operating conditions relevant to ride comfort analyses.

History

Received: 13 Apr 2026
Revised: 23 Jul 2026
Accepted: 14 Sep 2026
e-Available: 01 Oct 2026

Keywords

Friction modeling, Ride comfort, Shock absorber, Suspension friction, Vertical dynamics

Citation

Deubel, C., Meinck, J., Schramm, T., and Prokop, G., "Enhanced Suspension Friction Modeling for Vehicle Vertical Dynamics Simulation," *SAE Int. J. Veh. Dyn., Stab., and NVH* 11(1):2027, doi:10.4271/10-11-01-0005.

ISSN: 2380-2162
e-ISSN: 2380-2170

© 2027 Clemens Deubel, Johannes Meinck, Tobias Schramm, Günther Prokop. Published by SAE International. This Open Access article is published under the terms of the Creative Commons Attribution License (http://creativecommons.org/licenses/by/4.0/), which permits distribution, and reproduction in any medium, provided that the original author(s) and the source are credited.



1. Introduction

Virtualization of the vehicle development process is ongoing and will continue to gain importance in order to meet cost constraints and to enable the allocation of financial resources required for electrification and other associated transformations in the automotive sector [1]. Even during the early development stages, vehicle behavior must be replicated with a certain level of accuracy. Within the broad spectrum of vehicle functions, vehicle vertical dynamics represents a key discipline addressing the vibratory behavior of sprung and unsprung masses. Therefore, it largely determines the properties of road holding (safety) and ride comfort in terms of mechanical and acoustic vibrations perceived by the passenger. The forces transmitted through the suspension system fundamentally influence the vibration reaching the human–machine interfaces (e.g., hands, thighs, back), thereby contributing to overall comfort perception. In this context, the shock absorber (SA) is one of the most relevant components, as it decisively governs force transmission along the vertical load path. From an overall perspective, efficient and accurate design methodologies are required for proper virtual suspension design.

The SA is primarily characterized by damping (hydraulic force), stiffness (gas force, oil compressibility), and friction attributes. Numerous studies have addressed SA modeling with respect to stiffness and damping behavior [2–7], while relatively few have considered friction forces in greater detail [8, 9]. Over the past decade, semi-active and active SA systems have attracted significant research interest and demonstrated considerable potential for ride comfort improvement [10–13]. In such systems, damping forces can be actively adjusted to mitigate the classical trade-off between road holding and ride comfort. However, the friction force remains non-adjustable [14] and becomes increasingly relevant as the damping force is reduced. This aspect is particularly important for strut-type (MacPherson, MCP) front suspensions, in which SA friction varies substantially depending on the driving situation due to the inherent kinematic–kinetic configuration [15]. The side force (SF) acting on the SA is decisive [15–18] since the SA not only provides damping but also serves as a structural guiding element for the wheel carrier. The driving condition defines the suspension state both kinematically (spatial positions of suspension members, wheel, and SA) and kinetically (wheel forces and moments), thereby determining the instantaneous SF, which may vary considerably. For sufficiently large SF levels, SA friction can exceed the hydraulic force, particularly at low piston velocities below 50 mm/s.

While the overall modeling of SA forces is well established, no consensus exists regarding the required level of detail for friction modeling, which remains a complex and multi-domain phenomenon. Up to now, suspension (or SA) friction in vehicle vertical dynamics simulations has typically been represented by simplified models such as Coulomb, Stribeck, or Dahl formulations [19], as applied in [3, 14, 20–22]. A more detailed approach was presented by Angrick [23], who incorporated an amplitude-dependent effect within a Dahl-based formulation. Common simplifications—namely neglecting the dependency of friction on both velocity and normal force—may be acceptable for suspension systems exhibiting a limited variation in friction capacity (i.e., the value the friction force can assume at maximum upon entering the gross-sliding domain depending on the current conditions). However, this assumption is not valid for strut-type suspensions, as demonstrated in previous studies [15], where friction capacity strongly depends on the prevailing SF.

For this reason it is both legitimate and necessary to investigate friction modeling of MCP suspensions in greater detail. Owing to the enormous market share of this system among compact and mid-size vehicles, research in this field constitutes a highly relevant topic, leading to the central question: *Which friction model complexity is appropriate for a given application, considering modeling effort and achievable benefit relative to an idealized, highly detailed reference model*? A related question has been addressed in a recent research paper [24], where a friction model of variable detail was implemented for vehicle handling and a slow speed bump crossing simulation. This study shows that increased friction modeling complexity is necessary to accurately reproduce overall vehicle behavior. In a similar fashion, the present study focuses on ride comfort. Here, "ride comfort" is explicitly defined as the vertical mechanical vibration of the vehicle body (and associated roll and pitch vibrations) evaluated by objective measures.

To address the fact that there is no research considering the variable character of the friction force capacity in a full-vehicle vertical dynamics simulation, the following objectives are pursued:

- Development of an extended full-vehicle modeling framework combining kinematic and kinetic suspension analysis. This allows computing the instantaneous SF acting on the SA based on tire forces, moments, and suspension state, thereby enabling maneuver-dependent friction capacity modeling and application.
- Simulation of realistic driving scenarios—including cornering and lane change maneuvers across various vehicle speeds and road classes—to systematically evaluate the influence of friction model complexity on vehicle body and wheel vertical dynamics.
- Derivation of a recommendation regarding the appropriate level of friction modeling detail required for vertical dynamics (ride comfort) analysis.

The article is structured as follows. Section 2 presents in detail the modeling of the front axle (FA) vertical suspension path. It focuses on the experiment-based modeling of SA friction and compares three friction modeling approaches with respect to their influence on

the SA force signal. Section 3 presents the full-vehicle model, introducing the framework to calculate the instantaneous SF. Section 4 describes the vertical dynamics simulation setup and discusses the results in the time and frequency domains. Finally, Section 5 summarizes the conclusions.

2. Modeling of the FA Vertical Path

Regarding the vehicle under investigation, a VW Passat B8, the FA is the primary focus of this study, as it features an MCP suspension that is inherently subjected to SA SF, as discussed in the introduction. In order to study the friction effect in detail, the vertical suspension path should be modeled with high fidelity. This requirement comprises two dimensions:

1. The qualitative dimension ensures that established physical phenomena can occur within the model. In particular, it requires an appropriate representation of the top mount (TM), since only then can the sticking behavior of the SA, arising under high friction forces, be correctly reproduced in terms of body and wheel vertical dynamics, especially regarding eigenfrequency characteristics.
2. The quantitative dimension ensures an accurate magnitude of the individual suspension component forces. This is necessary to assess the friction force effect relative to the other force contributions on a physically consistent basis.

2.1. Instrumentation and Test Program

Accurate modeling of the vertical load path requires parameterization based on dedicated physical test rig experiments. Table 1 provides an overview of the investigated components, the corresponding test rigs, and the validation strategy according to the respective modeling complexity.

TABLE 1 Parameterization overview of the vertical path.

Vertical path element	Attributes	Test rig	Validation
Shock absorber, top mount	Stiffness, damping, friction	One-axis hydropulser	Yes
Coil spring	Stiffness		No
Anti-roll bar	Stiffness	Full-vehicle test rig (Suspension motion simulator)	No
Residual suspension	Friction		No
Tire	Stiffness, enveloping behavior	Tire test rig	No

© Clemens Deubel, Johannes Meinck, Tobias Schramm, Günther Prokop

A key experimental tool for component testing is a one-axis hydropulser, schematically shown in Figure A.1. Its hydraulic unit enables excitation along the vertical axis. For the SA configuration, the SA tube is actuated relative to a fixed piston rod. A controllable SF can be applied pneumatically via a coupling rod at the height of the piston rod thread, thereby replicating the load situation present in the real suspension. By definition, movement in the negative vertical direction corresponds to compression, whereas rebound denotes motion in the opposite direction. The test rig is also used for parameterization of the TM and the coil spring properties. Further test rig specifications can be found in Table A.1. The test program is depicted in Table A.2, while specific reference is made in the following sections.

With respect to the modeled forces described below, the terms “quasi-static,” “steady-state dynamic,” and “transient dynamic (also: non-steady-state dynamic)” are introduced as used throughout this work: quasi-static refers to measurements obtained at the lowest achievable excitation velocity and thus under conditions close to static equilibrium. Steady-state dynamic refers to measurements obtained under harmonic steady-state excitation with constant frequency and amplitude after transient effects have decayed. In contrast, transient dynamic denotes measurements obtained under varying excitation conditions or during non-steady operating states.

2.2. Modeling the SA

In a first step, the SA properties are modeled. The specimen is an SA of the VW Passat B8 (termed “Pas-3”), and properties are listed in Table A.3. In addition, a specialized valve-free specimen (“Pas-1”)—not experimentally investigated within the present study—is considered indirectly. Findings from a previous investigation [25] are partially utilized to support the parameterization of the currently tested specimen (“Pas-3”). Further details are provided below.

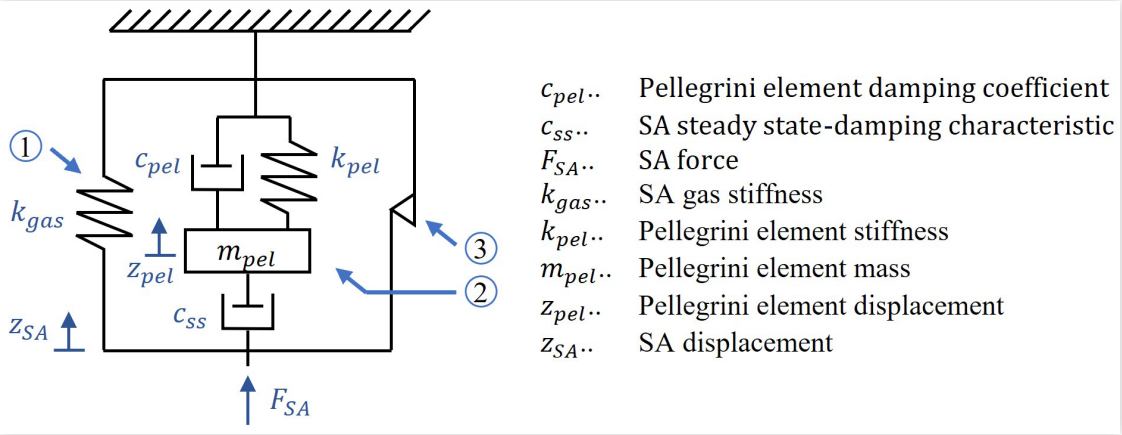
Figure 1 illustrates the overall model topology of the SA, comprising a gas spring force F_{gas} (1), the hydraulic force F_{hydr} (2), and friction force F_f (3). The total SA force F_{SA} is thus represented as the superposition of these contributions:

$$F_{SA} = F_{gas} + F_{hydr} + F_f \tag{1}$$

The individual elements are described in detail in the following sections. The model boundary conditions and objectives are as follows:

- A constant temperature is assumed; hence, temperature effects are not modeled.

FIGURE 1 Topology of the SA model: gas force (1), hydraulic force (2), friction force (3).



© Clemens Deubel, Johannes Meinck, Tobias Schramm, Günther Prokop

- High modeling accuracy is prioritized within a low amplitude and velocity range (approximately up to 20 mm and 500 mm/s), which is considered particularly relevant for analyzing SA friction effects. This follows the argument that the relative influence of friction decreases with deteriorating road conditions [21, 26], which are associated with higher excitation amplitudes and velocities.
- Valve dynamics and cavitation effects are neglected, as they become increasingly significant only at higher velocities [27].

2.2.1. Gas Force According to previous investigations on the valve-free specimen of the same type ("Pas-1") [25], the gas force is modeled as a spring with frequency-dependent stiffness. First, the static gas stiffness $k_{gas,stat}$ is determined for the actual specimen ("Pas-3") by regression analysis of the force–displacement characteristic under quasi-static excitation (0.5 mm/s sine cycle), evaluated within ±10 mm around the zero-crossing. This yields $k_{gas,stat}$ = 0.69 N/mm.

Direct dynamic measurements of the gas stiffness for "Pas-3" are not feasible due to the superimposed hydraulic forces. Therefore, the frequency-dependent amplification is represented by a sigmoid function $G_{gas}(f)$ derived from previous results obtained with the specimen ("Pas-1") in accordance with thermodynamic principles reported in [25]. The function assumes $G_{gas}(0) = 1$ and converges to $G_{gas}(f \geq 2\ \text{Hz}) \approx 1.345$.

$$G_{gas}\left(f\right) = \frac{c_1 + 1}{c_1 + e^{c_2 \cdot f}} = \frac{2.892 + 1}{2.892 + e^{-3.734\,\text{Hz}^{-1} \cdot f}} \tag{2}$$

Then, the dynamic stiffness $k_{gas,dyn}$ can be expressed as

$$k_{gas,dyn}\left(f\right) = k_{gas,stat} \cdot G_{gas}\left(f\right) \tag{3}$$

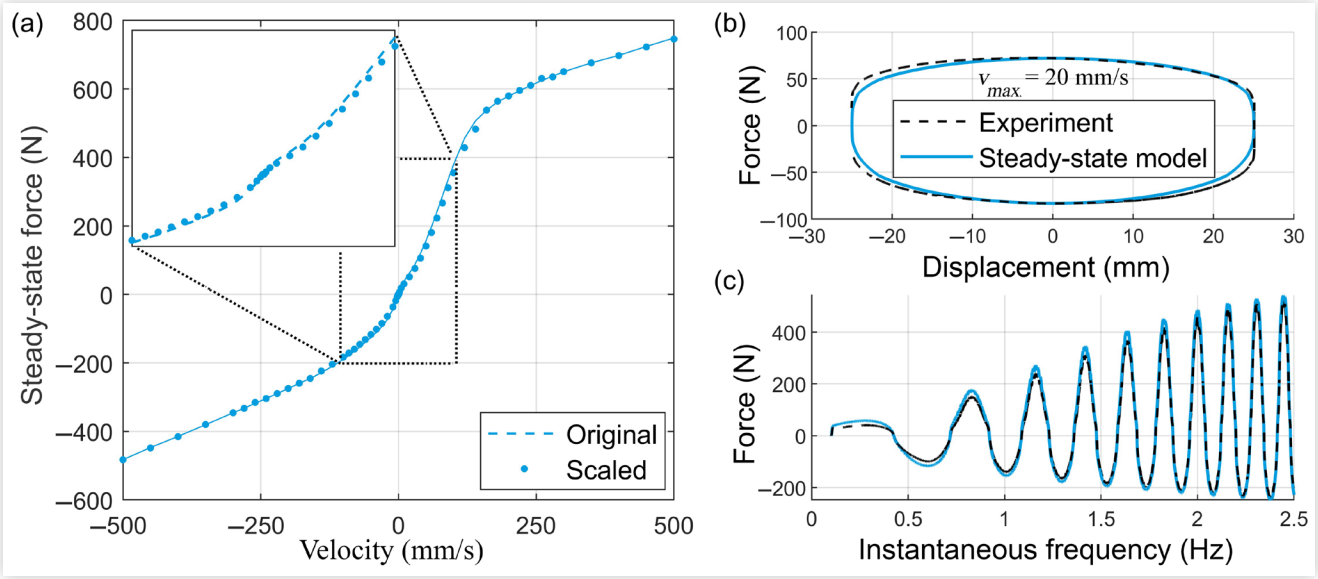
Furthermore, the gas preload force $F_{gas,pre}(K0)$ is determined. This leads to the total gas force:

$$F_{gas}\left(x_{SA}, f\right) = F_{gas,pre}\left(K0\right) + z_{SA} \cdot k_{gas,dyn}\left(f\right) \tag{4}$$

2.2.2. Hydraulic Force Several approaches to model the hydraulic SA force, including the dynamic force–velocity hysteresis caused by additional compressibility of oil and structural components, are reported in the literature. These approaches combine the steady-state characteristic with basic rheological elements, as in Maxwell or Pellegrini models [5–7], or apply transfer function–based concepts such as the Hammerstein model [3]. All three variants were implemented and evaluated. The Pellegrini and Hammerstein formulations provided the highest accuracy. The Pellegrini model, see Figure 1, can be interpreted as an extension of the Maxwell model, offering increased flexibility through the inclusion of an additional inertia element. A damping element is required to suppress high-frequency natural oscillations. Although the Hammerstein model exhibits advantages in computational efficiency and numerical stability—since no high series stiffness is required—the Pellegrini model was selected due to its superior overall performance.

All phenomenological dynamic formulations are based on the essential steady-state SA curve, built from the force response due to steady-state inputs (i.e., evaluating the force at the velocity maximum of each cycle, which could be more correctly termed a "quasi-steady-state" region, as it represents the moment that comes closest to steady-state velocity conditions). It is determined up to 500 mm/s (the relevant operating range of this study), using a refined velocity discretization, see TP2 (Table A.2). The measured force signal is corrected by subtracting the gas force and the *quasi-static* friction force obtained from the 0.5 mm/s cycle. Under this definition, hydraulic damping at 0.5 mm/s is assumed to be zero; the measured force consists solely of gas and friction

FIGURE 2 Steady-state force (a) and its application at 20 mm/s sine cycle (b) and sine sweep (c).



© Clemens Deubel, Johannes Meinck, Tobias Schramm, Günther Prokop

contributions. For higher velocity cycles, the velocity-dependent steady-state friction component—exceeding the quasi-static friction level—remains implicitly included in the signal. As separating this contribution from the hydraulic force is neither feasible nor required (see Section 2.2.3), it is attributed to the hydraulic force component.

Figure 2(a) shows the steady-state SA curve. Applying the steady-state force model in Figure 2(b) to the input signals reveals that the force during the transient phases (i.e., apart from the zero-crossing of the displacement near the maximum velocity) of the sine cycle up to approx. 100 mm/s is underestimated. Conversely, during sine sweep excitation [Figure 2(c)], the steady-state model overestimates the force within a comparable velocity range, defined here by the instantaneous sweep frequency. Therefore, opposing deviations are observed for harmonic steady-state and sweep excitations, which cannot be resolved by the previously mentioned model variants. However, since suspension excitation under real driving conditions is predominantly non-steady-state, the force response under sweep excitation is considered more relevant than under sine excitation. Thus, the identified deviations are compensated by applying a scaling factor, based on comparing the sweep and sine data specific to each velocity discretization. This adapted curve is visualized in Figure 2(a) and forms the basis for subsequent modeling.

In the next step, the parameters of the Pellegrini model are identified using a particle swarm optimization (PSO). Parameterization employs the previously introduced sweep signals and a red noise excitation, i.e., a random excitation with a power spectral density that decreases with frequency, approximately proportional to $1/f^2$. This signal aims to represent the energy distribution of a real road, containing frequency components from 0.2 Hz to 30 Hz. The differential equation, with symbols defined in Figure 1, is:

$$0 = m_{pel} \cdot \ddot{z}_{pel} + c_{ss}\left(\dot{z}_{pel} - \dot{z}_{SA}\right) \cdot \left(\dot{z}_{pel} - \dot{z}_{SA}\right) + k_{pel}\left(z_{pel}\right) \cdot z_{pel} + c_{pel} \cdot \dot{z}_{pel} \tag{5}$$

Based on the spring's deflection rate, the Pellegrini element force F_{pel} can be determined as

$$F_{pel} = c_{ss}\left(\dot{z}_{pel} - \dot{z}_{SA}\right) \cdot \left(\dot{z}_{pel} - \dot{z}_{SA}\right) \tag{6}$$

The spring's stiffness k_{pel} is defined as direction-dependent. In order to enable smooth switching of parameters at zero deflection, a sigmoid function is applied for transitioning the linear stiffness of compression k_{comp} and rebound k_{reb} directions. The parameter p_{tanh} controls the transition.

$$k_{pel}\left(x_{pel}\right) = \frac{k_{comp} + k_{reb}}{2} + \frac{k_{comp} + k_{reb}}{2} \cdot \tanh\left(p_{\tanh} \cdot x_{pel}\right) \tag{7}$$

The parameters determined by the PSO algorithm are listed in Table 2, and the accuracy of the modeled force is shown in Table 3. Accuracy is defined in terms of the root mean squared error (RMSE) and the normalized RMSE (NRMSE), which are both based on the difference $F_{exp,i} - F_{model,i}$ of the experimental and the modeled force of each data point i.

$$\mathrm{RMSE} = \sqrt{\frac{\sum_{i=1}^{N}\left(F_{exp,i} - F_{model,i}\right)^2}{N}} \tag{8}$$

TABLE 2 Parameterization of the Pellegrini model.

Parameter	Value	Unit
k_{comp}	992,000	N/m
k_{reb}	3,600,000	N/m
m_{pel}	2.37	kg
p_{tanh}	16,328	1/m
c_{pel}	700	N · s/m

© Clemens Deubel, Johannes Meinck, Tobias Schramm, Günther Prokop

$$\mathrm{NRMSE} = \sqrt{\frac{\sum_{i=1}^{N}\left(F_{exp,i} - F_{model,i}\right)^2}{N}} \Big/ \sqrt{\frac{\sum_{i=1}^{N} F_{exp,i}^{\,2}}{N}} \tag{9}$$

Figure 3 illustrates a representative time segment of the red noise signal. Under dynamic excitation, the series stiffness reduces the steady-state force and introduces a phase shift, resulting in a slightly delayed force build-up. The inertia element contributes to force reduction immediately after the force maximum. During optimization, the Pellegrini damping coefficient converges to the predefined lower boundary of 700 (N · s)/m, which is required to sufficiently damp the system eigenfrequencies.

Validation of the hydraulic force is performed according to TP4 (Table A.2), including a sweep signal with logarithmically decreasing amplitude and a measured real-road SA signal (containing well-maintained road segments, wavy segments, concrete slabs). Each test is repeated at least five times, and no model error is assigned as long as the model force remains within the variation of the experiment. The results (Table 4) demonstrate a significant accuracy improvement compared to the purely steady-state model. Improvements are particularly pronounced for time intervals with higher frequency components, where phase-related deviations dominate if not properly represented. Overall, the normalized error during parameterization and validation ranges between 5% and 10%, which is considered satisfactory for the intended application.

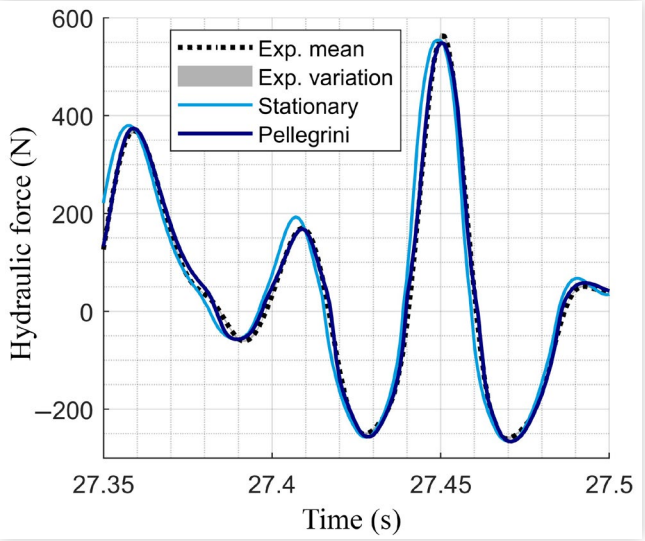
2.2.3. Friction Force Friction in the SA exhibits steady-state and transient tribological characteristics [25], with friction magnitude being primarily governed by relative velocity and SF. Both influences are strongly interrelated [25]. In a former study [25], a heuristic friction model was developed and validated using a valve-free SA, allowing friction to be investigated independently of hydraulic damping. The present work extends this approach to an

TABLE 3 Accuracy of the Pellegrini model.

Signal	RMSE (N)	NRMSE (%)
Sweep 10 mm	41.3	8.7
Sweep 4 mm	39.1	10.2
Red noise	15.5	5.4

© Clemens Deubel, Johannes Meinck, Tobias Schramm, Günther Prokop

FIGURE 3 Parameterized Pellegrini model results (red noise).



© Clemens Deubel, Johannes Meinck, Tobias Schramm, Günther Prokop

intact production SA ("Pas-3"), representing a substantially more realistic but also more challenging application case, as hydraulic damping and friction cannot be separated experimentally. Consequently, the original formulation requires adaptation and re-parameterization. The resulting model variants form the basis for the subsequent vehicle dynamics investigations and are therefore outlined below.

The heuristic model force $F_{f,h}$ constitutes a superposition of forces and contains three essential terms:

$$F_{f,h}\left(F_s\right) = F_{\sigma_0}\left(F_s = 0\right) + \left[F_{f,qs}\left(F_s\right) - F_{f,qs}\left(F_s = 0\right)\right] \cdot c_s\left(v_{ave}\right) \tag{10}$$

The first term, "$F_{\sigma_0}(F_s = 0)$," describes the steady-state dynamic friction force F_{σ_0} at zero SF F_s. It is provided by the steady-state element of the LuGre friction formulation [28] as follows:

$$F_{\sigma_0} = \sigma_0 \cdot z \tag{11}$$

$$\frac{dz}{dt} = v - \sigma_0 \cdot \frac{|v|}{F_{ss}\left(v\right)} \cdot z \tag{12}$$

The steady-state force $F_{ss}(v)$ is obtained from dynamic measurements, whereas the contact stiffness σ_0 is

TABLE 4 Results of validation of hydraulic force.

	RMSE (N)	NRMSE (%)	
Validation signal	Pellegrini	Pellegrini	Steady-state
Sweep 30 mm log.	9.2	5.6	16.2
Real-road SA signal	9.1	4.8	8.5

© Clemens Deubel, Johannes Meinck, Tobias Schramm, Günther Prokop

identified from quasi-static experiments. Further details regarding the formulation of $F_{ss}(v)$ are provided in [25]. The second term $[F_{f,qs}(F_s) - F_{f,qs}(F_s = 0)]$ constitutes an SF-dependent quasi-static component. It is described by Dahl's first-order differential equation [19]:

$$\frac{dF_{f,qs}}{dt} = \sigma_0 \cdot v \cdot \left(1 - \frac{F_{f,qs}}{F_c} \cdot sgn(v)\right)^{\beta} \tag{13}$$

The contact stiffness σ_0, the form parameter β, and the Coulomb force F_c (toward which the quasi-static force $F_{f,qs}$ converges upon entering the gross-sliding domain, therefore being equivalent to the formerly introduced term "friction capacity") are identified by fitting the model to quasi-static experimental force–displacement curves. A further key element is the dynamic scaling factor $c_s(v_{ave})$, which modifies the quasi-static component as a function of the average relative velocity v_{ave} over the preceding 100 ms. In this manner, the model captures the characteristic Stribeck-type behavior of steady-state friction, featuring a maximum at low characteristic velocities followed by a decrease at higher velocities. This trend is qualitatively similar irrespective of the magnitude of SF.

A key difference compared to the valve-free specimen investigated in [25] is that, for the intact SA ("Pas-3"), the steady-state dynamic friction contribution cannot be isolated experimentally from the hydraulic force. Consequently, this contribution is assumed to be implicitly contained within the measured hydraulic characteristic. The following modification therefore represents the central adaptation required for transferring the previously developed friction model to an intact production SA. The total SA force and the corresponding heuristic friction force become:

$$F_{SA} = F_{gas} + F_{hydr} + F_{f,h}(F_s) \tag{14}$$

$$F_{f,h}(F_s) = F_{f,qs}(F_s) \cdot c_s(v_{ave}) \tag{15}$$

The dynamic scaling factor was previously identified using the valve-free specimen of the same SA type ("Pas-1") and is transferred to the actual specimen ("Pas-3"). Both characteristics are shown in Figure B.1. Consequently, parameterization of the present model is limited to the quasi-static SF-dependent friction component $F_{f,qs}(F_s)$.

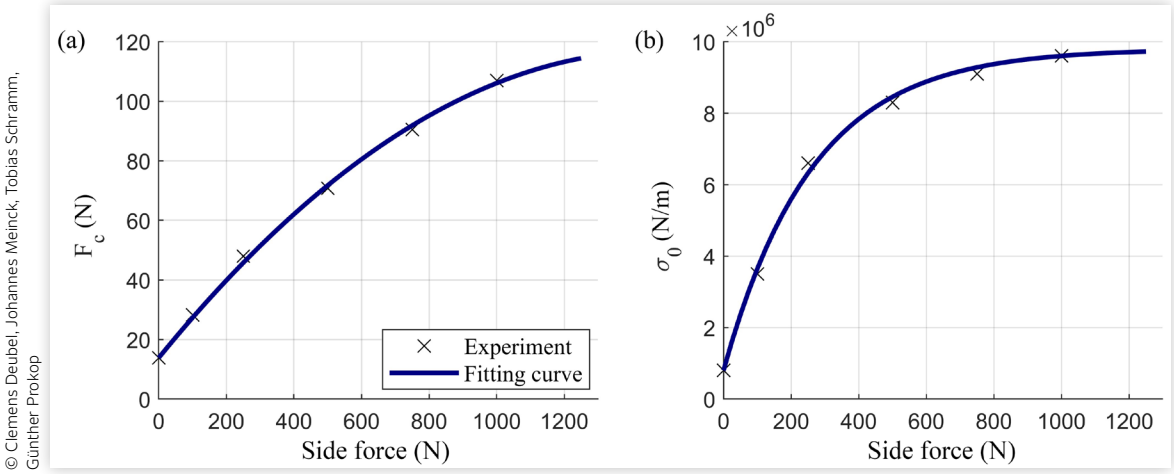
Quasi-static friction is determined following TP5 (Table A.2) under six SF levels and five static deflection levels (DLs). Deflection significantly influences the internal normal forces generated by the SF and thereby directly influences friction capacity. The nominal static DL is denoted as "$DL = K0_{SA}$" and corresponds to 118 mm (free piston rod length), representing the installed condition at vehicle standstill. During compression ("$K0_{SA}$-z"), normal forces decrease; during rebound ("$K0_{SA}$+z"), they increase, where z denotes the hydraulic cylinder position. Figure 4(a) and (b) illustrate the identified parameters F_c and σ_0. The Coulomb force F_c, defined as half the hysteresis width of the force–displacement diagram, increases degressively with SF and follows the quadratic formulation of Equation 16. The contact stiffness σ_0 is derived from the slope at force reversal points and is defined according to Equation 17. While F_c is deflection-dependent, as mentioned before, σ_0 can be defined as independent of deflection. The form parameter is set to $\beta = 2$.

$$F_c(F_s, K0_{SA}) = 13.8 + 0.139\,N^{-1} \cdot F_s - 0.000047\,N^{-2} \cdot F_s^{\,2} \tag{16}$$

$$\sigma_0(F_s) = \left[0.8 + 9.0 \cdot \left(1 - e^{-0.0038\,N^{-1} \cdot F_s}\right)\right] \cdot 10^6\ \mathrm{N/m} \tag{17}$$

Based on the fully parameterized heuristic formulation, model complexity can be systematically reduced to

FIGURE 4 Friction force at nominal static deflection level (a) and contact stiffness (b).



© Clemens Deubel, Johannes Meinck, Tobias Schramm, Günther Prokop

TABLE 5 Properties of friction model variants.

Model	Functional form $Ff_{,h,i}(F_s)$	Parameters	Characteristic	Abbreviation
$F_{f,h,1}$	$F_{f,qs}(0)$	$\sigma_0(0)$, $F_c(0)$, $\beta = 2$	No SF	"Nominal"
$F_{f,h,2}$	$F_{f,qs}(F_s)$	$\sigma_0(F_s, DL)$, $F_c(F_s, DL)$, $\beta = 2$	Including SF	"SF-dep., quasi-static"
$F_{f,h,3}$	$F_{f,qs}(F_s) \cdot c_s(v_{ave})$	$\sigma_0(F_s, DL)$, $F_c(F_s, DL)$, $\beta = 2$, $c_s(v_{ave})$	Including SF and dynamic scaling	"SF-dep., dynamic"

© Clemens Deubel, Johannes Meinck, Tobias Schramm, Günther Prokop

define simplified variants. Accordingly, three friction modeling variants are considered for their subsequent integration in the full-vehicle model, differing in the specification of the second and third terms of the original heuristic formulation. Note again that the steady-state friction contribution at zero SF (first term) remains implicitly included in all variants as part of the hydraulic force by definition. Equations 18a–18c describe the three variants, which are compared in Table 5.

$$F_{f,h,1}\left(F_s\right) = F_{f,qs}\left(0\right) \tag{18a}$$

$$F_{f,h,2}\left(F_s\right) = F_{f,qs}\left(F_s\right) \tag{18b}$$

$$F_{f,h,3}\left(F_s\right) = F_{f,qs}\left(F_s\right) \cdot c_s\left(v_{ave}\right) \tag{18c}$$

To account for continuously varying deflection during simulation and its effect on the friction force for a given SF, a procedure is developed that incorporates the relevant parameters during each time step of the simulation. As a result, a smooth, discontinuity-free friction force is obtained. This is explained in detail in Appendix C. In the next sections, the performance of the friction force models is assessed.

2.2.4. Validation of the SA Force The three partial SA forces are considered together under dynamic excitation and varying SF levels. The objective is to compare the three friction modeling variants and assess the performance of the heuristic modeling approach (benchmark model).

Validation is conducted using sinusoidal signals and two recorded test track signals. The first signal corresponds to a road class A segment, characterized by relatively low SA velocity and amplitude. The second exhibits higher velocity and amplitude and was recorded on a segment subjectively comparable to road class B, see TP6 (Table A.2). During excitation, the SF is modulated either stepwise or in the form of a ramp over a duration of 2.5 s, as exemplified for the 100 mm/s sine cycle in Figure 5. Both modulation types represent realistic driving conditions. Signal specifications are summarized in Table 6.

As can be seen from Figure 5(a) and (b), the increase of the experimentally measured force follows the trend of the SF. While friction model variant 3 captures the increase very accurately, variant 2 overestimates the friction force under elevated SF levels remarkably, as it neglects the mitigating influence of the dynamic scaling factor c_s. According to Table 6, the accuracy difference between variants 2 and 3 diminishes for low-frequency cycles (0.08/0.80 Hz), since the dynamic factor approaches unity and is therefore less influential. For the step input of Figure 5(c) and (d), the experimental friction force does not respond immediately but transitions smoothly. This is accounted for by applying a PT1 element to the SF input used in the friction calculation.

Overall, the complete heuristic model achieves very high accuracy, and the resulting total SA force closely matches experimental observations. Even under moderate SA velocities, such as during the 100 mm/s sine cycle or the road class B segment, the accuracy improvement compared to simplified variants is substantial. Variant 2 may still be considered an acceptable simplification when dynamic friction properties are unavailable, particularly at low velocities, and is characterized by a less extensive, quasi-static parameterization.

2.3. Modeling of the TM

The TM is a fundamental part of the MCP suspension model, as it allows the correct representation of alternating SA stick and slip modes and their effects on vertical dynamics, which may arise depending on the instantaneous amount of SA friction. SA stick leads to an increase in stiffness in the vertical path and consequently to a higher sprung mass eigenfrequency [26]. The MCP TM is typically designed as a two-path mount with distinct properties for the coil spring and the SA paths, see Figure 6.

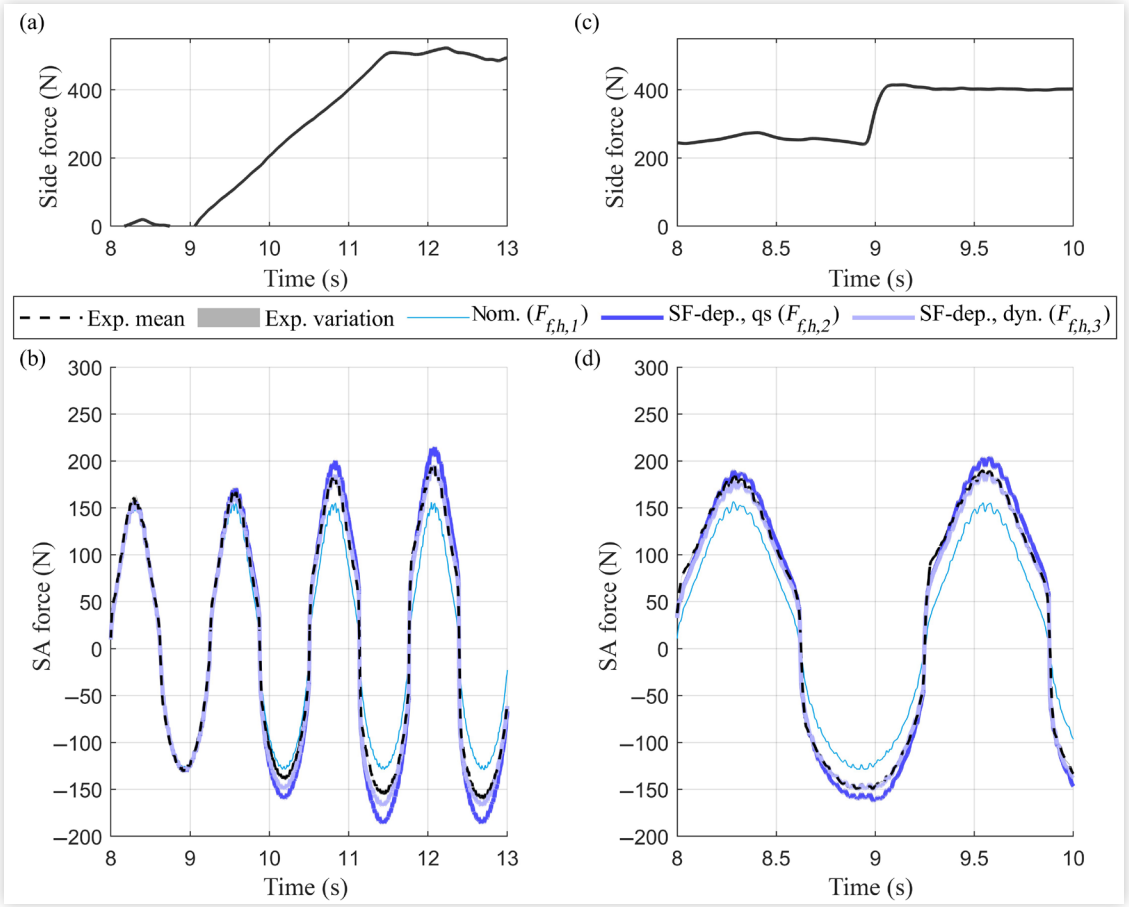
2.3.1. TM Coil Spring Path The TM spring path is parameterized using a linear spring element, based on quasi-static and dynamic test results from TP1 (Table D.1). The identified linearized quasi-static stiffness $k_{TM,coil,qs}$ and dynamic stiffness $k_{TM,coil,dyn}$ are:

$$k_{TM,coil,qs} \approx 7{,}900{,}000 \text{ N/m} \tag{19}$$

$$k_{TM,coil,dyn} \approx 1.65 \cdot k_{TM,coil,qs} \tag{20}$$

Since the TM stiffness is connected in series with the suspension coil spring ($k_{coil,FA} \approx 28{,}000$ N/m, refer to Table 7), its influence on the effective stiffness is limited. The difference in resulting effective stiffness when using quasi-static instead of dynamic TM stiffness is below 0.15% and therefore negligible. For reasons of simplicity, frequency-dependent effects and nonlinear properties of the TM coil spring path are therefore neglected; only the linearized quasi-static stiffness is considered.

FIGURE 5 Total SA force obtained through friction model variants under SF variation during signal: ramp input (a, b) and step input (c, d).



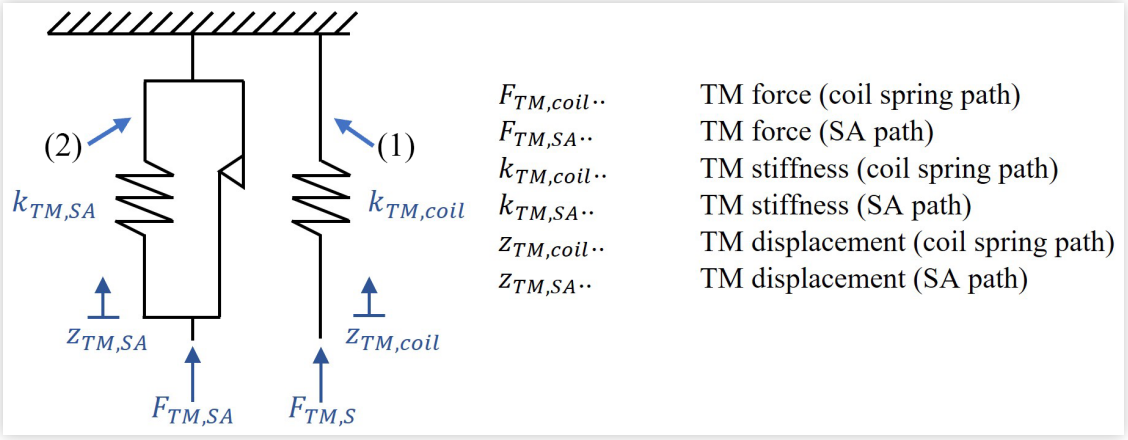
© Clemens Deubel, Johannes Meinck, Tobias Schramm, Günther Prokop

TABLE 6 Results of validation of hydraulic force.

Validation signal			RMSE (N)			NRMSE (%)		
Excitation	v_{max}	Side force	$F_{f,h,1}$	$F_{f,h,2}$	$F_{f,h,3}$	$F_{f,h,1}$	$F_{f,h,2}$	$F_{f,h,3}$
Sine 10 mm amp.	5 mm/s (0.08 Hz)	Ramp: 0 → 500 N	35.5	6.4	6.1	64.2	11.5	11.0
		Step: 250 → 400 N	41.2	5.8	5.9	64.8	9.1	9.2
		Step: 500 → 350 N	44.7	6.2	6.2	66.5	9.2	9.2
	50 mm/s (0.80 Hz)	Ramp: 0 → 500 N	27.7	12.0	5.9	23.2	10.0	4.9
		Step: 250 → 400 N	32.5	9.5	5.7	25.3	7.4	4.5
		Step: 500 → 350 N	36.3	12.0	6.2	27.4	9.0	4.7
	100 mm/s (1.60 Hz)	Ramp: 0 → 500 N	22.2	17.2	7.9	10.4	8.1	3.7
		Step: 250 → 400 N	25.4	15.9	7.3	11.5	7.2	3.3
		Step: 500 → 350 N	28.0	19.8	8.4	12.6	8.9	3.8
	150 mm/s (2.40 Hz)	Ramp: 0 → 500 N	18.2	22.0	10.8	6.1	7.4	3.6
		Step: 250 → 400 N	20.1	22.3	11.0	6.7	7.4	3.6
		Step: 500 →350 N	22.6	26.3	12.3	7.4	8.7	4.1
Road profile	44 mm/s (class A)	Step: 250 →400 N	35.0	8.7	8.0	49.2	12.3	11.3
		Step: 500 → 350 N	38.1	9.4	8.6	50.9	12.5	11.5
	328 mm/s (class B)	Step: 250 → 400 N	23.9	20.7	11.6	11.4	9.9	5.5
		Step: 500 → 350 N	25.9	22.9	12.4	12.3	10.9	5.9

© Clemens Deubel, Johannes Meinck, Tobias Schramm, Günther Prokop

FIGURE 6 Topology of the TM model: spring path (1), SA path (2).



© Clemens Deubel, Johannes Meinck, Tobias Schramm, Günther Prokop

2.3.2. TM SA Path The TM SA path is of greater relevance, resulting in specific requirements, but also in some simplifications:

- Representation of amplitude-dependent effects
- Consideration of frequency-related behavior
- Assumption of constant temperature
- Neglect of the Mullins effect, which is less pronounced under continuous excitation [29]

The complete test program is listed in TP2 (Table D.1). The final model topology consists of a nonlinear elastic (spring) element $F_{TM,SA,elast}$ and a friction element $F_{TM,SA,f}$:

$$F_{TM,SA} = F_{TM,SA,elast} + F_{TM,SA,f} \tag{21}$$

The elastic component is represented by a fifth-order polynomial, which accurately captures the progressive stiffness increase at higher excitation amplitudes, see Equation 22. The friction element is modeled using Berg's formulation [30]. Equations 23a–23c define the respective subfunctions depending on motion direction. The parameter $F_{TM,SA,f,max}$ defines the maximum friction force, while z_2 defines the characteristic displacement at which half of the maximum is reached. The variables F_{fs}, z_s describe the force and displacement at the beginning of each hysteresis loop and are updated at each motion reversal.

$$F_{TM,SA,elast} = \sum_{i=1}^{5} z_{TM,SA} \cdot k_{TM,SA,i} \tag{22}$$

$$F_{TM,SA,f} = \begin{cases} F_{fs} + \dfrac{z_{TM,SA} - z_s}{z_2 \cdot \left(1 - \dfrac{F_{fs}}{F_{TM,SA,f,max}}\right) + \left(z_{TM,SA} - z_s\right)} \cdot \left(F_{TM,SA,f,max} - F_{fs}\right) & z > z_s \quad (23a) \\ F_{fs} + \dfrac{z_{TM,SA} - z_s}{z_2 \cdot \left(1 + \dfrac{F_{fs}}{F_{TM,SA,f,max}}\right) - \left(z_{TM,SA} - z_s\right)} \cdot \left(F_{TM,SA,f,max} + F_{fs}\right) & z < z_s \quad (23b) \\ F_{fs} & z = z_s \quad (23c) \end{cases}$$

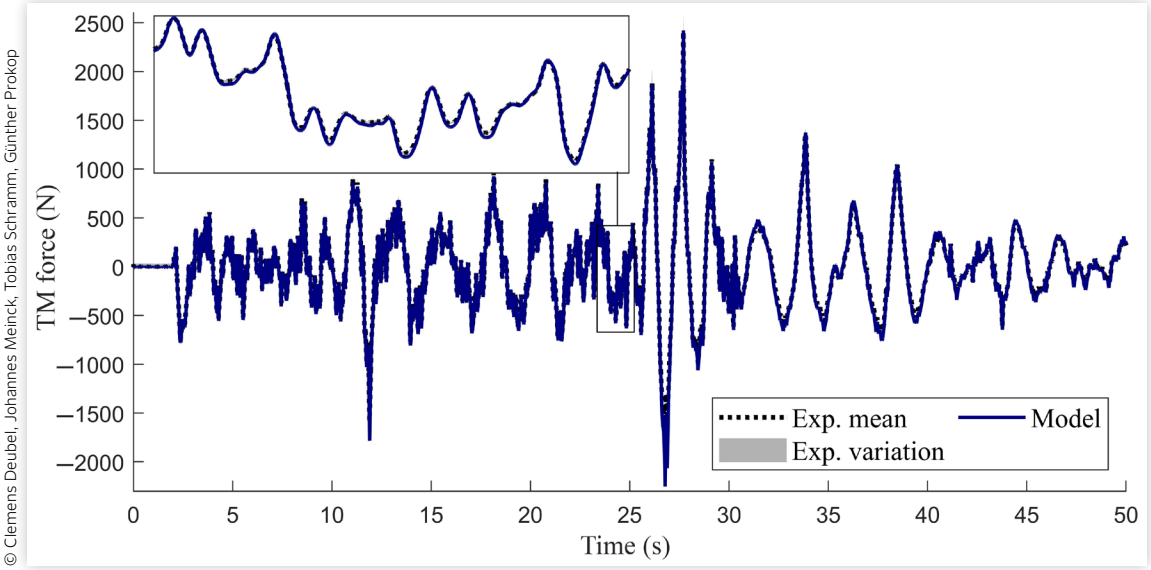
TABLE 7 Remaining FA suspension parameters.

Parameter	Value	Unit	Description
$F_{c,susp,FA}$	31.4	N	Remaining suspension friction (Dahl element: Coulomb friction coefficient, contact stiffness, form parameter)
$\sigma_{o,susp,FA}$	400,000	N/m	
$\beta_{susp,FA}$	2	—	
$k_{coil,FA}$	27,900	N/m	Coil spring vertical stiffness (linear)
$k_{arb,FA}$	19,900	N/m	TCP-related stiffness of anti-roll bar (linear), per Δ-vertical displacement FL–FR

© Clemens Deubel, Johannes Meinck, Tobias Schramm, Günther Prokop

Real-road measurements indicate that TM excitation predominantly occurs within a displacement range up to approximately 3 mm and velocity levels up to 100 mm/s under severe excitation. Spectral analysis reveals that the power spectral density of the excitation follows a $1/f^2$ decrease. Initially, additional viscous elements—implemented as Maxwell or spring-pot elements [31]—were considered but yielded no increased accuracy compared to a simple combination of a spring and a friction element. Since quasi-static high-amplitude testing of the TM damper path is not representative of real operating conditions (large TM displacements presuppose high SA forces and thus inherently dynamic excitation), parameters are identified using dynamic excitation signals: a red noise signal, a sine sweep (0.5 mm amplitude, 0.1–25 Hz), and singular sinusoidal tests. Parameters are estimated using a PSO algorithm and are listed in Table D.2. The NRMSE during parameterization reaches 3.0–4.2%, indicating a high modeling accuracy (see Table D.3).

FIGURE 7 Validation of TM SA path on recorded displacement profile (excerpt).



© Clemens Deubel, Johannes Meinck, Tobias Schramm, Günther Prokop

The model is validated using a recorded TM displacement profile and two additional sine sweeps. Validation results (see Table D.3 and Figure 7) confirm satisfactory accuracy with NRMSE ranging from 1.9% to 7.3%. Overall, the experimentally observed TM behavior exhibits negligible frequency dependency within the considered range up to 30 Hz. The proposed modeling topology therefore provides an easy-to-parameterize, computationally efficient representation while maintaining high accuracy.

2.4. Modeling of Remaining Suspension Friction, Coil Spring, Anti-Roll Bar

In addition to the friction of the SA, the friction of the remaining FA suspension is considered. While SA friction is governed by the SF and therefore depends on the suspension's kinematic and kinetic state, the friction of the remaining suspension components is assumed to be constant. In other words, a fixed friction capacity is adopted for these elements. The front suspension is characterized using the full-vehicle test rig described in [15]. To determine the minimum suspension friction, the tire lateral force is modulated to minimize the SA SF. The measurements are conducted under roll excitation, i.e., with anti-phase wheel inputs on the left and right sides, thereby engaging the anti-roll bar. Under these conditions, the measured friction comprises the friction of the remaining suspension components (primarily the combined friction of the suspension and anti-roll-bar bushings) as well as the nominal unloaded SA friction under simplified conditions (e.g., neglecting amplitude-dependent effects). Since the nominal SA friction is known from prior characterization, the friction parameters of the remaining suspension can be directly identified (Table 7).

The coil spring is another relevant element of the MCP suspension, as it is intentionally designed to generate specific SF levels [32, 33]. A method to determine the horizontal coil spring forces has previously been presented [15]. The corresponding characteristics are shown in Figure E.1.

The anti-roll bar is modeled as a linear vertical stiffness acting at the unsprung masses. It generates a force proportional to the relative vertical displacement between the left and right wheels. Note that with respect to the SA SF, the simplification is made that the anti-roll bar couple rod force is not applied to the strut.

3. Modeling of the Full Vehicle

The detailed front suspension models are subsequently integrated into a full-vehicle simulation framework. The underlying framework is derived from a previously developed, more comprehensive five-mass vehicle model [24] by deliberately removing physical effects that are not required for the present study, while retaining relevant characteristics for vertical dynamics investigations. The present work extends this framework by introducing the enhanced front suspension modeling described in the preceding sections. The modeling assumptions and simplifications follow the approach of Löhe [34] and are summarized below:

- The vehicle body is a torsionally rigid body.
- With the exception of the TM–piston rod connection, suspension components are modeled as pure force elements. All body-mounted component masses (e.g., seats, engine, interior equipment) are lumped into the vehicle body sprung mass and are therefore not represented as separate masses.

- Rotational motions (pitch, roll, and yaw) occur about the center of gravity (CoG).
- The CoG is laterally symmetric; the small measured lateral offset is neglected.
- Suspension forces act purely vertically on the body, independent of its instantaneous orientation.
- Unsprung masses vibrate purely in the z-direction. Wheel kinematics are not considered.
- Front and rear suspension motion ratios are assumed constant and independent of wheel travel; vehicle measurements confirm this assumption within the investigated deflection range.
- The investigated suspension travel range is sufficiently small to neglect bump and rebound stops.
- Apart from the TM, elastomer bushings and auxiliary spring rates are not modeled.
- Gravity acts vertically on all bodies; road slope and roll of the body are not considered.

Further simplifications concern the road excitation, the tire enveloping behavior, and longitudinal dynamics:

- The road excitation is defined purely in the vertical direction; however, longitudinal tire forces resulting from acceleration, braking, rolling resistance, and aerodynamic drag are still considered. Left and right wheel sides are excited independently. Rear-wheel excitation is delayed according to the current vehicle speed in relation to the wheelbase. The road height is generated according to the ISO 8608 standard [35], using a fitted road height power spectral density (PSD) with exponent $w = 2$.
- Tire enveloping is modeled using two 2D elliptical cams proposed by Schmeitz [36], which are parameterized with the original tires on a tire test rig. The model acts as a geometric filter providing an effective road height, from which vertical and longitudinal tire forces are derived. The vertical tire force is computed from the tire stiffness and the tire deflection, the latter being defined as the difference between the vertical wheel displacement and the mean effective tire deformation. The tire contact patch length, defined as a function of vertical force, is a main parameter affecting the effective tire deformation.
- The vehicle follows a prescribed target velocity profile representing the driver input. A PID controller computes the required longitudinal driving or braking force from the velocity error. Consequently, longitudinal vehicle motion results from the applied wheel forces in accordance with Newton's second law. No drivetrain dynamics or tire longitudinal slip are modeled. Driving forces are applied at the front wheels only (front-wheel drive), whereas braking forces are distributed across all wheels according to the instantaneous dynamic wheel load transfer.
- External forces: Aerodynamic drag and rolling resistance are included, requiring compensation by appropriate driving forces.

3.1. Overall Model Topology

The full-vehicle model is based on a mathematical five-mass formulation, as visualized in Figure 8, extended by two additional masses representing the piston rods of the front suspension SAs. The vehicle body has six degrees of freedom (DoF), while each wheel has one vertical DoF (plus one rotational DoF around the y-axis, being of minor interest). The piston rods of the front left (FL) and front right (FR) wheel corners each introduce one vertical DoF. In total, the model therefore comprises 12 relevant DoFs.

The equations of motion of the vehicle body are described by Equations 24–29. Here, $F_{x,i}$, $F_{y,i}$, $M_{z,i}$ denote the longitudinal and lateral wheel forces and the overturning moment at the TCP. $F_{susp,b,i}$ denote the (vertical) suspension forces at the body. At the FA, these body-side suspension forces differ from the corresponding wheel SFs $F_{susp,w,i}$ due to the interposed piston rod mass. This distinction is addressed in the subsequent section.

$$\ddot{x}_{veh} = \frac{F_{x,FL} + F_{x,FR} + F_{x,RL} + F_{x,RR} - F_{roll} - F_{aero}}{m_b + 2 \cdot m_{w,FA} + 2 \cdot m_{w,RA}} + \dot{\psi}_b \cdot \dot{y}_b \cong \ddot{x}_b \tag{24}$$

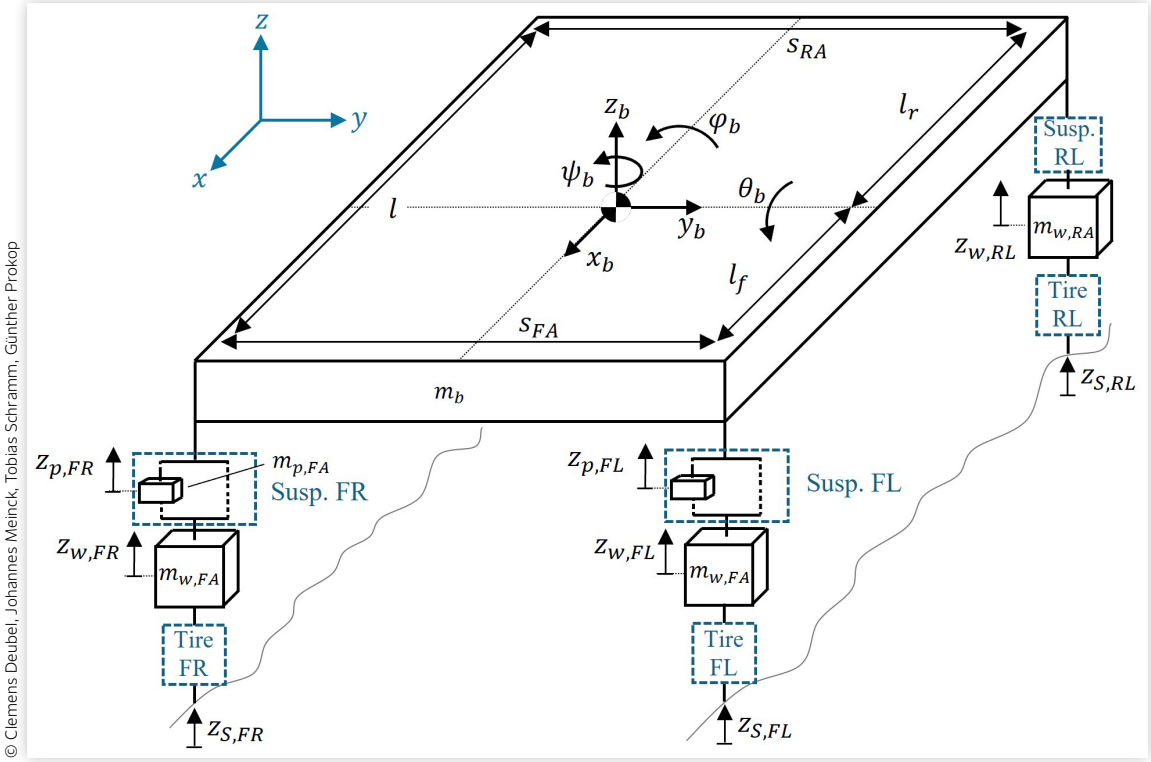
$$\ddot{y}_{veh} = \frac{F_{y,FL} + F_{y,FR} + F_{y,RL} + F_{y,RR}}{m_b + 2 \cdot m_{w,FA} + 2 \cdot m_{w,RA}} - \dot{\psi}_b \cdot \dot{x}_b \cong \ddot{y}_b \tag{25}$$

$$\ddot{z}_b = \frac{-F_{susp,b,FL} - F_{sups,b,FR} - F_{susp,b,RL} - F_{suspb,RR} - m_b \cdot g}{m_b} \tag{26}$$

$$\begin{aligned} \ddot{\varphi}_b \cdot J_{xx} &= F_{y,FL} \cdot \left(z_{b,FL} - z_{w,FL}\right) + F_{y,FR} \cdot \left(z_{b,FR} - z_{w,FR}\right) \\ &+ F_{y,RL} \cdot \left(z_{b,RL} - z_{w,RL}\right) + F_{y,RR} \cdot \left(z_{b,FR} - z_{w,FR}\right) \\ &- \left(F_{susp,b,FL} - F_{susp,b,FR}\right) \cdot \frac{s_{FA}}{2} - \left(F_{susp,b,RL} - F_{susp.b,RR}\right) \cdot \frac{s_{RA}}{2} \end{aligned} \tag{27}$$

$$\begin{aligned} \ddot{\theta}_b \cdot J_{yy} &= -F_{x,FL} \cdot \left(z_{b,FL} - z_{w,FL}\right) - F_{x,FR} \cdot \left(z_{b,FR} - z_{w,FR}\right) \\ &- F_{x,RL} \cdot \left(z_{b,RL} - z_{w,RL}\right) - F_{x,RR} \cdot \left(z_{b,FR} - z_{w,FR}\right) + \left(F_{susp,b,FL} + F_{susp,b,FR}\right) \cdot l_f \\ &- \left(F_{susp,b,RL} + F_{susp,b,RR}\right) \cdot l_r + M_{y,FL} + M_{y,FR} + M_{y,RL} + M_{y,RR} \end{aligned} \tag{28}$$

FIGURE 8 Visualization of the full-vehicle model.



© Clemens Deubel, Johannes Meinck, Tobias Schramm, Günther Prokop

$$\ddot{\psi}_b \cdot J_{zz} = \left(-F_{x,FL} + F_{x,FR}\right) \cdot \frac{s_{FA}}{2} + \left(-F_{x,RL} + F_{x,RR}\right) \cdot \frac{s_{RA}}{2} + \left(F_{y,FL} + F_{y,FR}\right) \cdot l_f - \left(F_{y,RL} + F_{y,RR}\right) \cdot l_r + M_{z,FL} + M_{z,FR} + M_{z,RL} + M_{z,RR} \tag{29}$$

Note that to obtain the roll and pitch motions $\ddot{\varphi}_b$, $\ddot{\theta}_b$, respectively, the displacement z_b denotes the current position of the body (CoG), therefore including the current position change resulting from Equation 26 plus the reference CoG height h_{CoG}.

$$z_b = \iint \ddot{z}_b + h_{CoG} \tag{30}$$

The equations of motion of the wheels $i = [FL, FR, RL, RR]$ are given by Equation 31:

$$\ddot{z}_{w,i} = \frac{\left(F_{susp,w,i} - F_{z,i} - m_{w,i} \cdot g\right)}{m_{w,i}} \tag{31}$$

The parameters of the full vehicle are listed in Table 8.

3.2. Suspension Topology Overview

The suspension topologies of the FA and rear axle (RA) are shown in Figure 9. The RA suspension force comprises SA force with steady-state force–velocity characteristic ($F_{SA,RA}$), linear coil spring force ($F_{coil,RA}$), linear anti-roll bar force ($F_{arb,RA}$), and Dahl-formulated suspension friction ($F_{f,susp,RA}$). The RA suspension force is equal regarding its effect on the body b (Equation 32) and the wheel w (Equation 33), respectively. The RA suspension properties are summarized in Table 9.

$$F_{susp,b,RA} = F_{SA,RA} + F_{coil,RA} + F_{arb,RA} + F_{f,susp,RA} - \frac{m_b \cdot l_f}{2 \cdot l} \cdot g \tag{32}$$

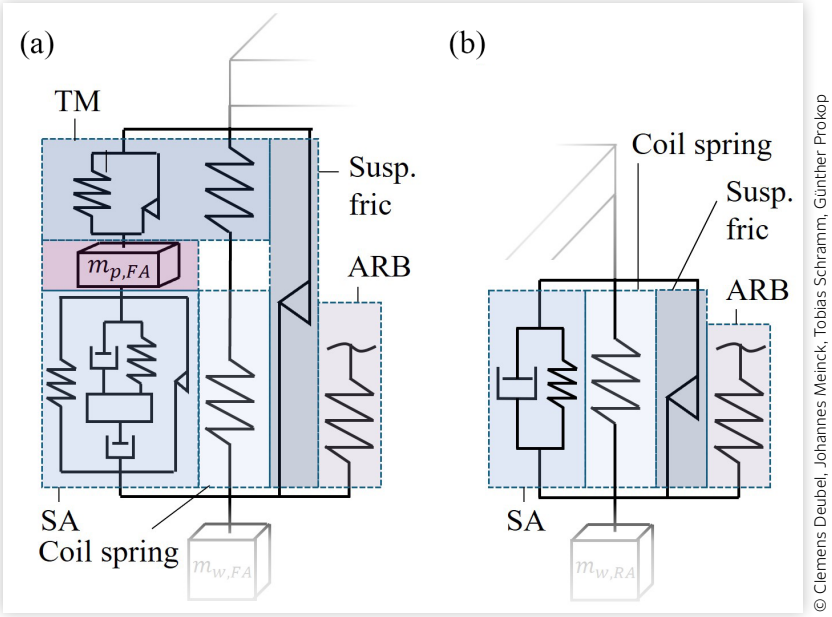
$$F_{susp,w,RA} = F_{susp,b,RA} \tag{33}$$

TABLE 8 Full-vehicle parameters.

Parameter	Value	Unit	Description
h_{CoG}	0.568	m	CoG height
l	2.791	m	Wheelbase
l_f/l_r	1.168/1.623	m	Distance CoG–FA/–RA
s_{FA}/s_{RA}	1.584/1.568	m	Track width FA/RA
m_b	1342	kg	Sprung mass
$m_{w,FA}/m_{w,RA}$	47/46	kg	Unsprung mass FA/RA
J_{xx}	520	kg·m²	Roll inertia (vehicle body)
J_{yy}	3038	kg·m²	Pitch inertia (vehicle body)
J_{zz}	3360	kg·m²	Yaw inertia (entire vehicle)

© Clemens Deubel, Johannes Meinck, Tobias Schramm, Günther Prokop

FIGURE 9 Suspension topology at FA (a) and RA (b).



© Clemens Deubel, Johannes Meinck, Tobias Schramm, Günther Prokop

The FA force components have been elaborated in Section 2 namely the SA force ($F_{SA,FA}$), TM force of SA path ($F_{TM,SA,FA}$), coil spring force ($F_{coil,FA}$), anti-roll bar force ($F_{arb,FA}$), and remaining suspension friction ($F_{f,susp,FA}$). Owing to the selected suspension topology, the suspension forces acting at the body and wheels differ at the FA due to the implementation of the TM in combination with the piston rod mass m_p.

$$F_{susp,b,FA} = F_{TM,SA,FA} + F_{coil,FA} + F_{arb,FA} + F_{f,susp,FA} - \frac{m_b \cdot l_r}{2 \cdot l} \cdot g \tag{34}$$

$$F_{susp,w,FA} = F_{SA,FA} + F_{coil,FA} + F_{arb,FA} + F_{f,susp,FA} - \frac{m_b \cdot l_r}{2 \cdot l} \cdot g \tag{35}$$

While the wheel side is directly subjected to the SA force, the body side is loaded by the TM force. These two forces are not identical owing to the inertia force of the piston rod mass. The equations of motion of the piston rods of the wheel corners i = [FL,FR] (neglecting gravity) are thus as follows:

$$\ddot{z}_{p,i} = \frac{F_{TM,FA} - F_{SA,FA}}{m_{p,i}} = \frac{\left(F_{susp,b,i} - F_{susp,w,i}\right)}{m_{p,i}} \tag{36}$$

Another essential component is the tire, which is modeled by a Kelvin–Voigt element consisting of a linear spring (k_w = 295,000 N/m) and a linear damper (c_w = 50 (N · s)/m, estimated from [37]). Tire enveloping is incorporated as described in the modeling simplifications above. Based on the instantaneous effective road height and its velocity, the vertical tire force $F_{z,i}$ is calculated that is needed to solve Equation 31.

TABLE 9 RA suspension properties.

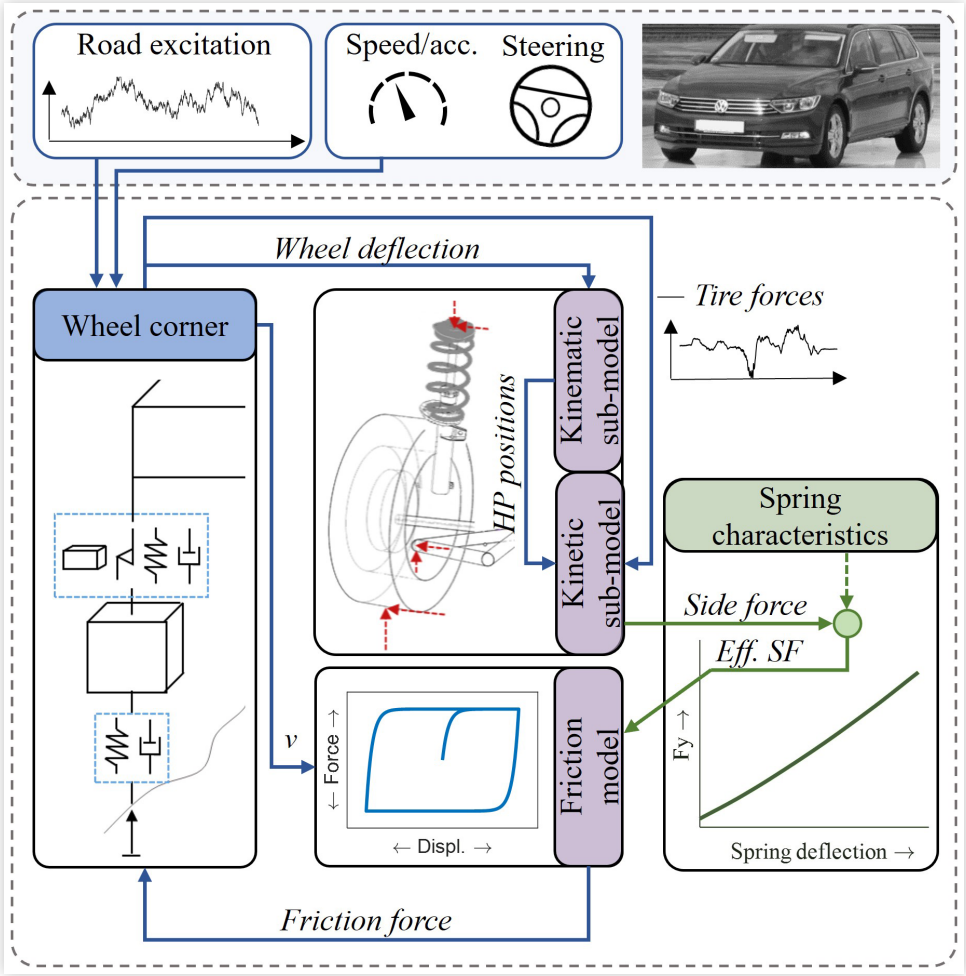
Parameter	Value	Unit	Description
$F_{c,susp,RA}$	60.5	N	Rear suspension friction (Dahl element: Coulomb friction coefficient, contact stiffness, form parameter)
$\sigma_{0,susp,RA}$	320,000	N/m	
$\beta_{susp,RA}$	2	—	
$k_{coil,RA}$	52,600	N/m	Coil spring vertical stiffness (linear) and transmission ratio
$i_{coil,RA}$	0.68	—	
$k_{SA,RA}$	110	N/m	SA gas stiffness
$i_{SA,RA}$	0.93	—	SA transmission ratio
$k_{arb,RA}$	10,000	N/m	TCP-related stiffness of anti-roll bar (linear), per Δ-vertical displacement RL–RR

© Clemens Deubel, Johannes Meinck, Tobias Schramm, Günther Prokop

3.3. Calculation of Instantaneous SF

As outlined in Section 2, SA friction is primarily governed by relative velocity, current deflection, and—most importantly—the magnitude of SF. The SF acting at the TM of the MCP suspension results from the interaction of tire forces and suspension kinematics. The instantaneous wheel position relative to the vehicle body defines the spatial configuration of the suspension members and thereby affects the horizontal force equilibrium at the TM. This contribution is referred to as the kinematic SF $F_{s,kin}$. The kinematic SF is superimposed by the spring-induced SF, yielding the effective SF $F_{s,eff}$ experienced by the SA.

FIGURE 10 Workflow to calculate instantaneous SF and friction force.



© Clemens Deubel, Johannes Meinck, Tobias Schramm, Günther Prokop

This effective SF increases the internal normal forces within the SA and thus directly determines its friction capacity. The entire SF mechanism is explained in greater detail in [15].

To account for this mechanism, each FA wheel corner is equipped with a coupled kinematic–kinetic sub-model that provides a time-resolved SF input to the friction model. The procedure is illustrated in Figure 10 and summarized briefly below. At each time step, the relative vertical deflection between body and wheel is known and provided to the kinematic sub-model. This sub-model contains a database of the spatial kinematic point (hardpoint, HP) coordinates of all suspension members as a function of wheel deflection. From this information, the current 3D kinematic configuration is reconstructed and passed to the kinetic sub-model. The kinetic sub-model represents the suspension from a force–moment equilibrium perspective and consists of 12 equations. In addition to the HP positions, the vertical and horizontal tire forces of each wheel corner, resulting from the driving maneuver (acceleration, cornering, etc.), serve as inputs. Solving the equation system, the suspension forces at the HP interfaces can be calculated, refer to [38] for additional details. Of particular relevance is the spatial TM force, which includes the kinematic SF component. The sub-model has previously been validated against a commercial multi-body simulation environment [38] and showed an average error of 1.8% of the calculated SF regarding application of longitudinal and lateral tire forces, as well as overturning moments.

Finally, the kinematic SF is superimposed with the spring-induced SF (deflection-dependent) to obtain the effective SF. After passing a PT1 element (see Section 2.2.4), it is forwarded to the friction model block. The instantaneous friction force is then calculated as described in Section 2.2.3 and fed back to the wheel corner model as a suspension force. Note that the effect of high-frequency SF oscillation, which might potentially exist in reality owing to horizontal vibration of the unsprung masses or due to spatial road excitation, is neither accounted for by the framework nor by the friction model block.

4. Vertical Dynamics Simulation

4.1. Test Cases

With the established model, simulations are conducted according to the maneuver clusters presented in Table 10. Cluster 1 represents straight driving at constant speeds (30–100 km/h) and is characterized by nearly constant SA SF. Cluster 2 extends this scenario by introducing steering input (Figure F.1), leading to additional lateral tire forces and thus elevated SF levels. Cluster 3 focuses on longitudinal dynamics using a prescribed velocity profile (Figure F.2). Some of these maneuvers additionally include a superimposed steering input, resulting in elevated SF levels. All simulations are carried out with a sampling rate of 20 kHz using an explicit fourth-order Runge–Kutta (ode4) formula. Variable-step implicit solvers did not provide computational advantages, as friction-dominated systems with rapidly varying numerical stiffness lead adaptive solvers to operate close to their minimum step size [39].

4.2. Results on SF and Friction Capacity

The analysis first examines the evolution of SF and the associated SA friction capacity. For straight driving at constant speed (cluster 1), both SF and friction capacity remain nearly constant. In contrast, lateral tire forces generated during steering maneuvers (cluster 2) induce pronounced SF variations. Figure 11 (lower row) shows results for road class A for four vehicle speeds, exemplarily for the FL wheel.

At the beginning of the maneuver, the nominal effective SF level of approx. 300 N is present, due to the imbalance between the lateral SF component and the spring-induced SF (cf. Figure E.1). For the FL wheel, this nominal SF is directed toward the vehicle outside. During a left turn [Figure 11(a) and (b)], the lateral tire force, acting through the suspension kinematics, generates an additional SF component in the same direction, resulting in increasing SF levels and friction capacities with increasing cornering severity. During a right turn, however, the tire force–induced SF acts in the opposite direction. At low cornering speeds, this contribution partially compensates the nominal SF, leading to reduced effective SF levels. As the vehicle speed increases, the lateral tire forces increase accordingly and eventually exceed the nominal SF contribution, causing the effective SF to reverse direction. Consequently, the magnitude of the SF increases again despite the change in sign.

At 50 km/h [Figure 11(c) and (d)], higher lateral tire forces and rebound deflection during left turns lead to higher internal normal forces and thus increased friction capacity. In contrast, right turns at this speed are characterized by pronounced compression, which reduces the internal normal forces and therefore the friction capacity despite substantial tire lateral forces and elevated SF magnitudes.

At 70 and 100 km/h [Figure 11(e) and (h)], wheel load transfer becomes increasingly important. During left turns, the FL wheel acts as the inner wheel and experiences a reduction in wheel load. As a result, the increase in lateral tire force is limited despite the higher cornering speed. Although rebound conditions promote higher internal normal forces [15], the resulting SF remains comparatively low. During right turns, the FL wheel acts as the outer wheel and is subjected to significantly increased wheel loads. Together with the larger lateral tire forces required for cornering, this leads to high SF levels. However, the concurrent compression state partially counteracts this effect, resulting in friction capacities similar to those observed for left turns.

Similar trends are observed for road classes B and C and for the FR wheel (Figure G.1). These results demonstrate that friction capacity is governed by the coupled interaction of wheel load, tire forces, and suspension kinematics, such that stronger cornering does not necessarily lead to higher friction levels.

Regarding the combined acceleration and steering maneuvers of cluster 3 (Figure 12), similar mechanisms apply. During straight-lane acceleration and braking [Figure 12(a)–(d)], higher SF levels are observed compared to cluster 1. Acceleration shifts the suspension into rebound, increasing friction capacity, whereas braking induces compression and reduces it. When steering is superimposed [Figure 12(e)–(h)], TCP forces are superimposed, further increasing friction capacity, particularly during simultaneous acceleration and left steering. During the right turn, although the SA SF reaches a maximum, pronounced compression as a consequence of braking reduces friction capacity.

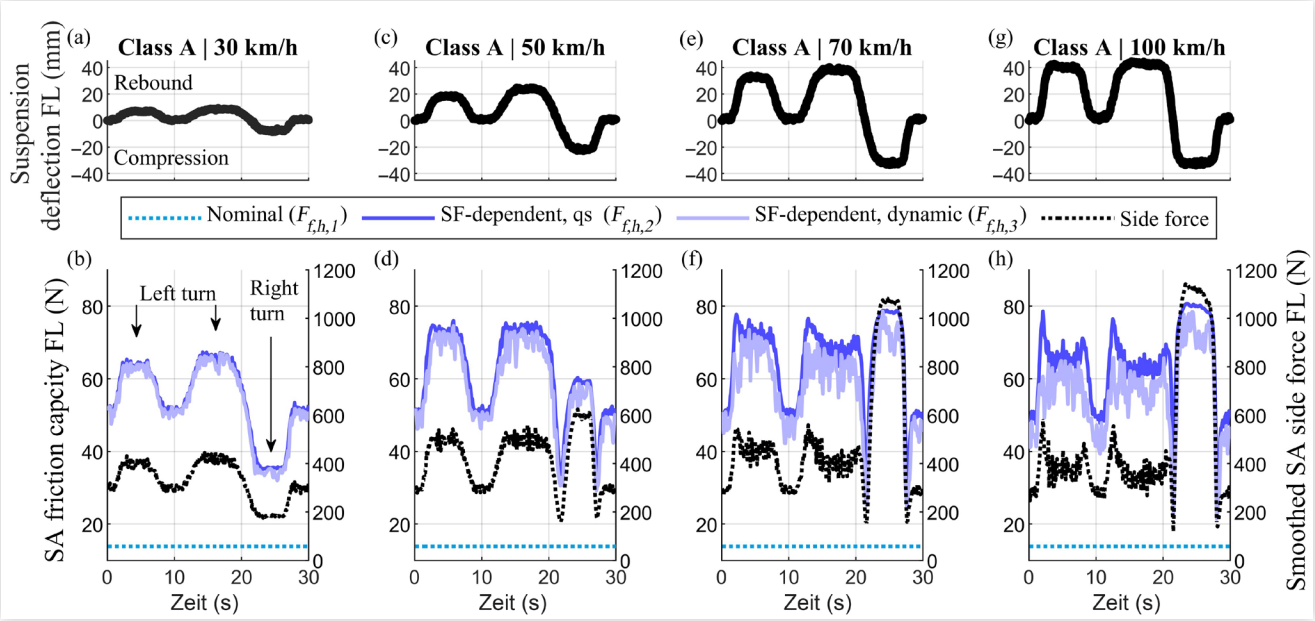
Figure 12 also highlights the deviation between the less complex friction model $F_{f,h,2}$ and the benchmark

TABLE 10 Simulative test plan.

Cluster	Vehicle speed	Steering	Road profile	Comment
1	Constant: 30 | 50 | 70 | 100 km/h	None (straight lane)	Classes A | B | C	Class C up to 50 km/h
2		Steering according to profile		
3	Speed according to profile	None (straight lane); steering according to profile	Classes A | B	—

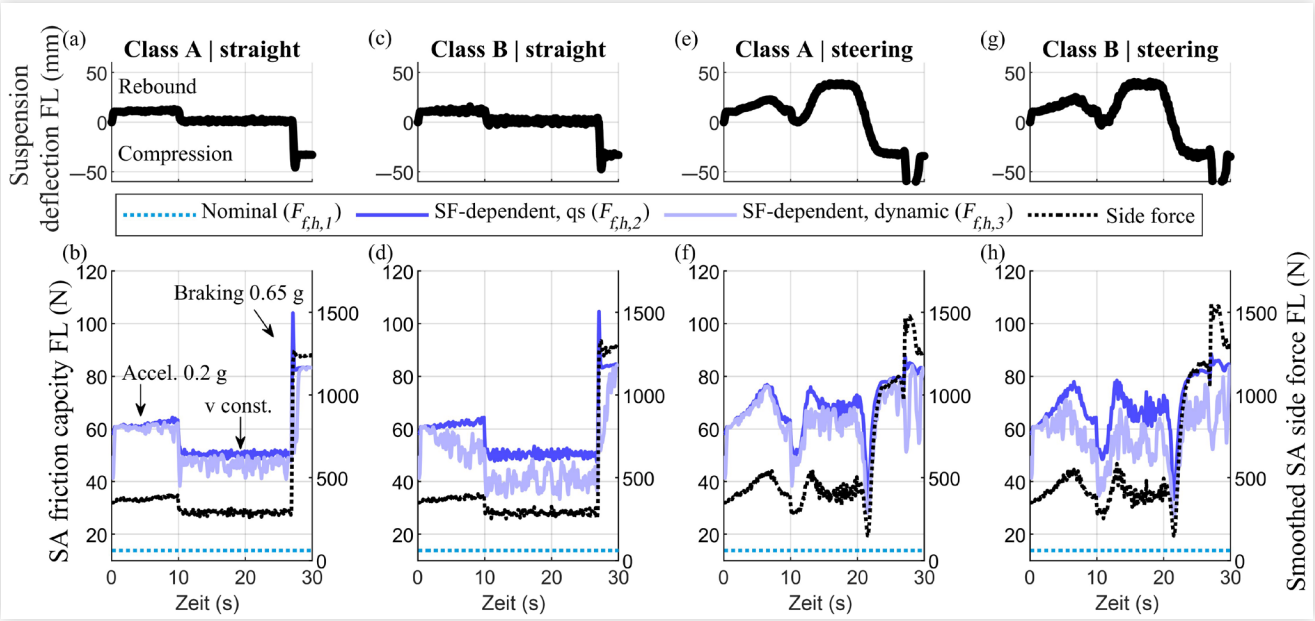
© Clemens Deubel, Johannes Meinck, Tobias Schramm, Günther Prokop

FIGURE 11 FL: SA SF and friction capacity (lower row) plus suspension deflection (upper row) during steering at vehicle speeds 30 km/h (a, b), 50 km/h (c, d), 70 km/h (e, f), and 100 km/h (g, h) on road class A.



© Clemens Deubel, Johannes Meinck, Tobias Schramm, Günther Prokop

FIGURE 12 FL: SA SF and friction capacity (lower row) plus suspension deflection (upper row) during acceleration (a–d) and during combined acceleration and steering (e–h).



© Clemens Deubel, Johannes Meinck, Tobias Schramm, Günther Prokop

TABLE 11 SF and friction capacity characteristics of the maneuvers (average of FL, FR).

Maneuver		$\overline{F_c}$ (N)		
Road | vel. | steering	$\overline{F_s}$ (N)	$F_{f,h,2}$	$F_{f,h,3}$	S
A | 30 km/h | none	287.9	50.2	49.1	0.97
A | 50 km/h | none	286.8	50.1	47.9	0.94
A | 70 km/h | none	285.3	50.0	46.6	0.91
A | 100 km/h | none	283.7	50.0	44.9	0.87
B | 30 km/h | none	287.9	50.2	45.2	0.86
B | 50 km/h | none	286.6	50.0	41.9	0.78
B | 70 km/h | none	284.8	49.9	39.4	0.72
B | 100 km/h | none	282.5	49.7	37.1	0.65
C | 30 km/h | none	286.6	49.7	37.5	0.66
C | 50 km/h | none	284.3	49.2	34.3	0.56
A | 30 km/h | profile	272.1	47.9	46.8	0.96
A | 50 km/h | profile	377.1	55.6	52.4	0.92
A | 70 km/h | profile	514.3	62.6	56.8	0.87
A | 100 km/h | profile	566.8	64.3	56.5	0.83
B | 30 km/h | profile	272.6	48.0	43.1	0.86
B | 50 km/h | profile	389.9	56.4	47.2	0.79
B | 70 km/h | profile	539.3	63.3	50.2	0.72
B | 100 km/h | profile	596.6	65.1	48.4	0.64
C | 30 km/h | profile	273.4	47.9	36.0	0.66
C | 50 km/h | profile	394.1	56.3	39.4	0.56
A | profile | none	425.6	59.7	56.1	0.89
B | profile | none	429.7	59.8	50.2	0.77
A | profile | profile	604.9	69.7	64.1	0.86
B | profile | profile	632.4	70.7	58.4	0.75

© Clemens Deubel, Johannes Meinck, Tobias Schramm, Günther Prokop

model $F_{f,h,3}$. On smooth roads (class A), both models show strong agreement, especially in steady-state conditions. However, during transient phases (beginning/end of acceleration, braking, or steering) the simplified model overestimates the instantaneous friction capacity because it neglects the velocity-dependent reduction represented by the enhanced model. The same can be seen on road class B during acceleration: as the vehicle speed gradually increases, excitation severity and SA velocity rise, leading to increased deviations. Table 11 summarizes characteristic values and shows the similarity index S of all the maneuvers, which is defined as a normalized Euclidean distance based on the L2 norm [40]:

$$S = 1 - \frac{\sqrt{\sum_{i=1}^{N} \left(F_{f,h,2,i} - F_{f,h,3,i}\right)^2}}{\sqrt{\sum_{i=1}^{N} F_{f,h,3,i}^{\,2}}} \tag{37}$$

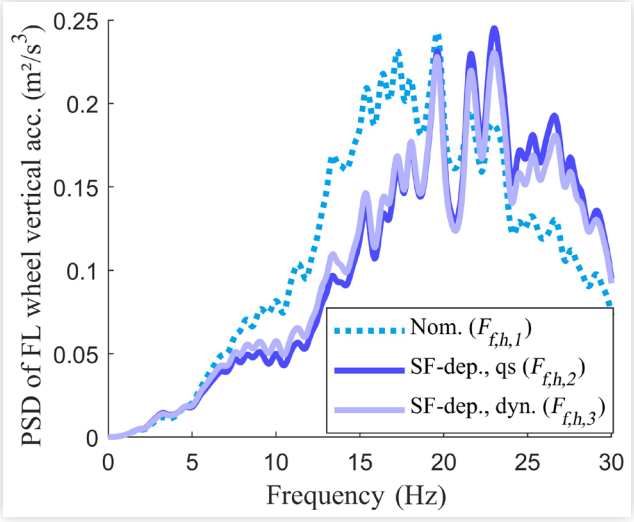
Empirically, maneuvers with $S \geq 0.9$ (light gray in Table 11) exhibit sufficient similarity, indicating that the less complex model $F_{f,h,2}$ provides an adequate simplification of the benchmark model $F_{f,h,3}$. For $0.85 < S < 0.9$ (dark gray with white font), agreement remains acceptable but begins to deteriorate. Below this threshold, friction capacity is strongly velocity-dependent and significant deviations occur. In summary, simplified modeling by $F_{f,h,2}$ is sufficient at low speeds and on high-quality roads, whereas dynamic conditions (high speeds, rough roads) require the enhanced model $F_{f,h,3}$ for accurate prediction of friction capacity.

4.3. Results on Vertical Dynamics in the Frequency Domain

The simulation maneuvers are evaluated from a ride comfort perspective, first using the PSDs of the FL wheel (Figure 13) and vehicle body (Figure 14) for road class A, where friction effects are most pronounced. For both the wheel and the vehicle body, distinct resonance frequencies are not immediately apparent. For the wheel, the analytically calculated eigenfrequency is around 13 Hz, yet this frequency is not clearly pronounced in Figure 13. Instead, the nominal friction model exhibits a PSD maximum near 16 Hz. One reason is the non-negligible magnitude of friction in the SA and the remaining suspension, imposing a stiffness-increasing effect. Another reason lies in the idealized road excitation according to ISO 8608 [35]. As the road height PSD follows an exponent $w = 2$, the corresponding PSD decreases with $1/f^2$ (red noise). However, in the time domain, acceleration $a_s(t)$ and displacement $z_s(t)$ are related quadratically, with $\hat{z}, \omega, \varphi$ being the amplitude, angular frequency, and phase, respectively:

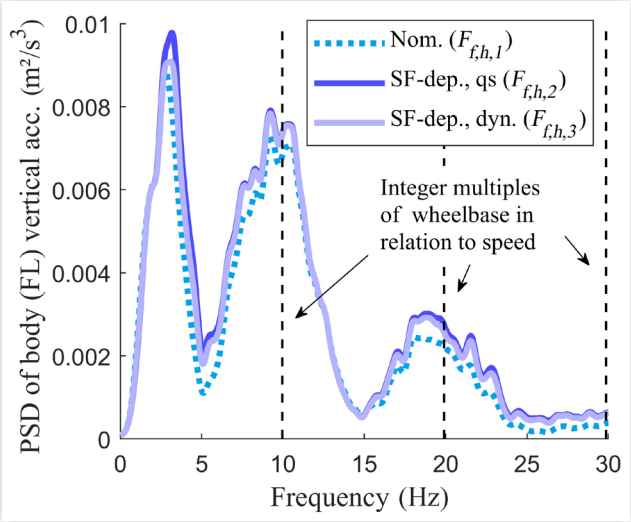
$$a_s(t) = \ddot{z}_s(t) = -\omega^2 \cdot \hat{z} \cdot \sin(\omega t + \varphi) \tag{38}$$

FIGURE 13 PSD of FL wheel vertical acceleration on road class A, 100 km/h.



© Clemens Deubel, Johannes Meinck, Tobias Schramm, Günther Prokop

FIGURE 14 PSD of vehicle body (FL) vertical acceleration on road class A, 100 km/h.



© Clemens Deubel, Johannes Meinck, Tobias Schramm, Günther Prokop

Therefore, the Fourier-transformed $A_s(\omega)$ and the auto PSD $S_{a_s a_s}(\omega)$ become, respectively:

$$A_s(\omega) = -\omega^2 \cdot Z_s(\omega) \Leftrightarrow S_{a_s a_s}(\omega) = \omega^4 \cdot S_{z_s z_s}(\omega) \quad (39)$$

Thus, the acceleration PSD increases proportionally to f^2, causing the wheel acceleration PSD to be dominated by the excitation, which masks its natural resonance (eigenfrequency). Additional simulations with harmonic excitation confirm the theoretical eigenfrequency. For the more enhanced models containing higher friction values, significantly less spectral power is observed in the wheel eigenfrequency range around 13 Hz due to the damping effect of friction. Conversely, higher PSD values appear in the 22–25 Hz range, reflecting the stiffening of the vertical path, as previously discussed in [26]. In fact, two distinct, idealized eigenfrequencies can be associated with the stick and slip states of the SA. For low friction (nominal model), slip dominates and the SA operates freely. The corresponding *slip eigenfrequency* of the FL wheel $f_{w,FA.slip}$ can be estimated as:

$$f_{w,FA.slip} \approx \frac{1}{2\pi} \cdot \sqrt{\frac{k_{coil,FA} + k_w}{m_{w,FA}}} \approx 13.3\ \text{Hz} \quad (40)$$

In the case of high friction, assuming the SA to stick entirely (neglecting contact stiffness), the coil spring stiffness and the SA path TM stiffness act in parallel [26], and the *stick eigenfrequency* is estimated as:

$$f_{w,FA.stick} \approx \frac{1}{2\pi} \cdot \sqrt{\frac{k_{coil,FA} + k_{TM} + k_w}{m_{w,FA}}} \approx 23.4\ \text{Hz} \quad (41)$$

Regarding the vehicle body (FL wheel corner), the PSD in Figure 14 shows noticeable attenuations at 5, 15, 25 Hz, etc. These result from the coupled heave–pitch motion in relation to vehicle speed and wheelbase. For the two-axle vehicle, the time delay between FA and RA excitation is $\Delta t = l/v_x$, with l being the wheelbase and v_x being the (longitudinal) vehicle speed. Under sinusoidal excitation and assuming identical suspension characteristics of the FA and RA, pure heave motion occurs when the phase $\omega\Delta t$ between FA and RA excitation equals integer multiples n of 2π [41, 42].

$$\omega\Delta t = n \cdot 2\pi \quad (42)$$

Reformulated with Ω denoting the angular spatial frequency, L denoting the road wavelength:

$$\omega\Delta t = \omega \cdot \frac{l}{v_x} = \Omega \cdot l = \frac{2\pi \cdot l}{L} \quad (43)$$

In other words, pure heave appears when the wheelbase equals the road wavelength or n multiples thereof [41]:

$$l = n \cdot L \quad (44)$$

In this case, pitch motion becomes zero. For the sinusoidal excitation with the wavelength L, this appears only when the condition of Equation 44 is fulfilled. For real roads constituting a superposition of numerous wavelengths, the same observations are possible at the frequencies f_n. Rewriting Equation 42 provides:

$$f_n = \frac{n}{\Delta t} = \frac{n \cdot v_x}{l} \quad (45)$$

Similar observations can be made regarding the pitch motion. Presuming the CoG to be in the middle of the FA and the RA, pitch acceleration reaches a maximum and CoG heave acceleration becomes zero, leading to the attenuation mentioned earlier. This happens at frequencies of:

$$\omega\Delta t = (2n-1)\pi \Leftrightarrow f_n = \frac{(n-0.5) \cdot v_x}{l} \quad (46)$$

Therefore, the corresponding amplification and attenuation frequencies increase with vehicle speed. In a realistic model, the CoG is not exactly centered between the FA and RA, and front and rear suspension properties differ. Consequently, heave and pitch will be permanently present. Nevertheless, the characteristic curve form ("garland curve" [41, 42]) remains clearly visible in Figure 14. This interaction makes it difficult to isolate the primary body eigenfrequencies, which occur at:

$$f_{b,slip} \approx \frac{1}{2\pi} \cdot \sqrt{\frac{k_{coil,FA} \cdot k_w}{m_{b,FA} \cdot (k_{coil,FA} + k_w)}} \approx 1.3\,\text{Hz} \quad (47)$$

$$f_{b,stick} \approx \frac{1}{2\pi} \cdot \sqrt{\frac{(k_{coil,FA} + k_{TM}) \cdot k_w}{m_{b,FA} \cdot (k_{coil,FA} + k_{TM} + k_w)}} \approx 3.7\,\text{Hz} \quad (48)$$

Despite this masking, a higher PSD level in the range from 3 Hz (stick eigenfrequency region) up to the wheel eigenfrequency range (≈13 Hz), therefore covering the intermediate range, can be observed for the models $F_{f,h,2}$, $F_{f,h,3}$. This can be attributed to the damping effect of the friction force in sliding, which usually increases body acceleration outside the primary body modes and is therefore detrimental to ride comfort. Above the wheel eigenfrequency, PSD levels again exceed those of the nominal model for the same reason. The friction effect (and thus the model differences between $F_{f,h,1}$ and $F_{f,h,2/3}$) becomes more pronounced at lower vehicle speeds. As road-induced velocity and acceleration decrease, friction-related effects dominate more strongly, particularly in the combined body resonance and intermediate frequency ranges. Conversely, on road classes B and C, the relative influence of friction diminishes.

Overall, this analysis highlights that the effects of the friction model are more difficult to distinguish in more sophisticated vehicle models compared to abstracted models, such as the quarter-car model. Nevertheless, the two main effects of friction as illustrated by the three model variants are underlined:

- A stiffness-related effect, which can shift wheel and body eigenfrequencies toward higher values (stick behavior).
- A damping-like effect, which increases body vertical acceleration apart from the body eigenfrequency and thus impairs ride comfort (sliding behavior).

Similar observations can be made for the roll and pitch accelerations not shown here. The longitudinal, lateral, and yaw accelerations are small in comparison and therefore not analyzed further.

4.4. Results on Objective Ride Comfort in the Time Domain

The vertical, roll, and pitch acceleration signals are now evaluated in the time domain. In this study, they are interpreted as objective *discomfort* measures, meaning that higher values indicate higher discomfort levels. This simplification is deliberate, acknowledging that comfort, i.e., the absence of discomfort [43], is a multilayered topic: Comfort encompasses traditional domains (such as noise or climate) [44], as well as emerging aspects including motion sickness [45] or trust in driving functions [46, 47], in addition to the vibratory component. Multiple transmission paths (directions, vehicle–passenger interfaces) contribute differently to an overall comfort perception [48], which is inherently subjective and likely nonlinear [48, 49]. These aspects are beyond the scope of the present work. Instead, the acceleration signals are first weighted according to the ISO 2631 standard [48], accounting for human sensitivity. The weighted accelerations of vertical body, roll and pitch acceleration are then analyzed using two complementary approaches:

(i) An integral RMS is calculated over the full signal to quantify a *mean discomfort ratio* between friction model variants.

(ii) A running RMS (RRMS) with a 1 s window size and 90% overlap to capture the maximum *instantaneous discomfort* level and its temporal variation for each of the implemented friction models. By comparing the friction model variants, a *maximum instantaneous discomfort ratio* can be determined.

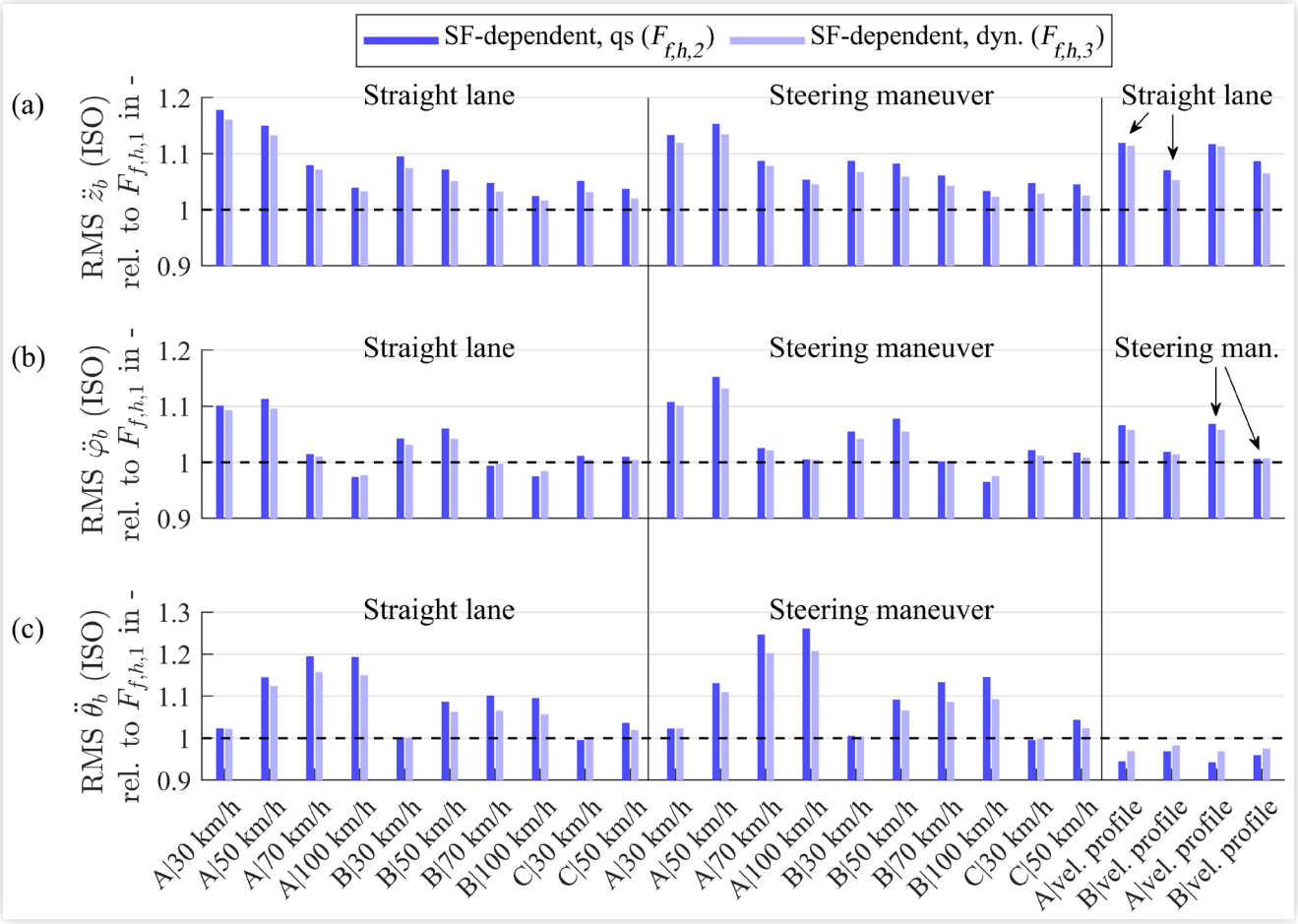
To quantify the influence of friction modeling, the resulting RMS and RRMS values are expressed as discomfort ratios relative to the reference friction model. It should be noted that the present evaluation does not constitute a comprehensive ride comfort assessment according to ISO 2631. Instead, the weighted vehicle body accelerations are used as objective discomfort indicators to quantify the relative influence of the implemented friction models. Passenger contact point accelerations (e.g., seat, backrest, and feet) are not considered, as these quantities are not represented by the vehicle model. Longitudinal, lateral, and yaw accelerations were also evaluated but showed negligible sensitivity to the implemented friction model variants. This is consistent with suspension friction acting primarily through the vertical force path, while lateral and yaw responses are dominated by the driving maneuver itself. Consequently, the presented metrics are intended for the comparative assessment of friction model variants rather than for determining absolute ride comfort levels.

Figure 15 presents the RMS values of vertical body acceleration $\ddot{z}_b$ (a), roll acceleration $\ddot{\varphi}_b$ (b), and pitch acceleration $\ddot{\theta}_b$ (c) for the models including SF-dependent friction ($F_{f,h,2}$, $F_{f,h,3}$) relative to the nominal model ($F_{f,h,1}$), i.e., the relative discomfort ratio. Absolute RMS values are summarized Table H.1.

For the vertical acceleration during straight-lane driving, the relative discomfort ratio decreases with increasing vehicle speed and road roughness. Friction is therefore most influential at low speeds and on high-quality roads, where hydraulic damping forces are comparatively small. Since the models $F_{f,h,2}$, $F_{f,h,3}$ account for increased friction capacity due to SF, vertical discomfort rises. This is attributed to (i) a shift of body resonance toward higher frequencies with greater ISO 2631 weighting considering human sensitivity (particularly regarding inner organs [50, 51]) and (ii) increased vibration below the wheel eigenfrequency due to reduced wheel–body isolation.

The more severe the excitation, the less influential the friction modeling effect. Sticking becomes less likely, minimizing the eigenfrequency shift. Furthermore, hydraulic damping gains increasing relevance. For road classes A (30–70 km/h) and B (30 km/h), discomfort

FIGURE 15 Relative RMS of enhanced friction models relative to nominal model for vertical body acceleration (a), roll acceleration (b), and pitch acceleration (c).



© Clemens Deubel, Johannes Meinck, Tobias Schramm, Günther Prokop

increases exceeding 10% indicate that enhanced friction models are justified when high accuracy of vertical dynamics is required. The difference between $F_{f,h,2}$ and $F_{f,h,3}$ grows with increasing excitation severity, particularly on road classes B and C, due to velocity-dependent scaling. However, friction contributes less to the overall force (see Figure I.1) and thus loses importance.

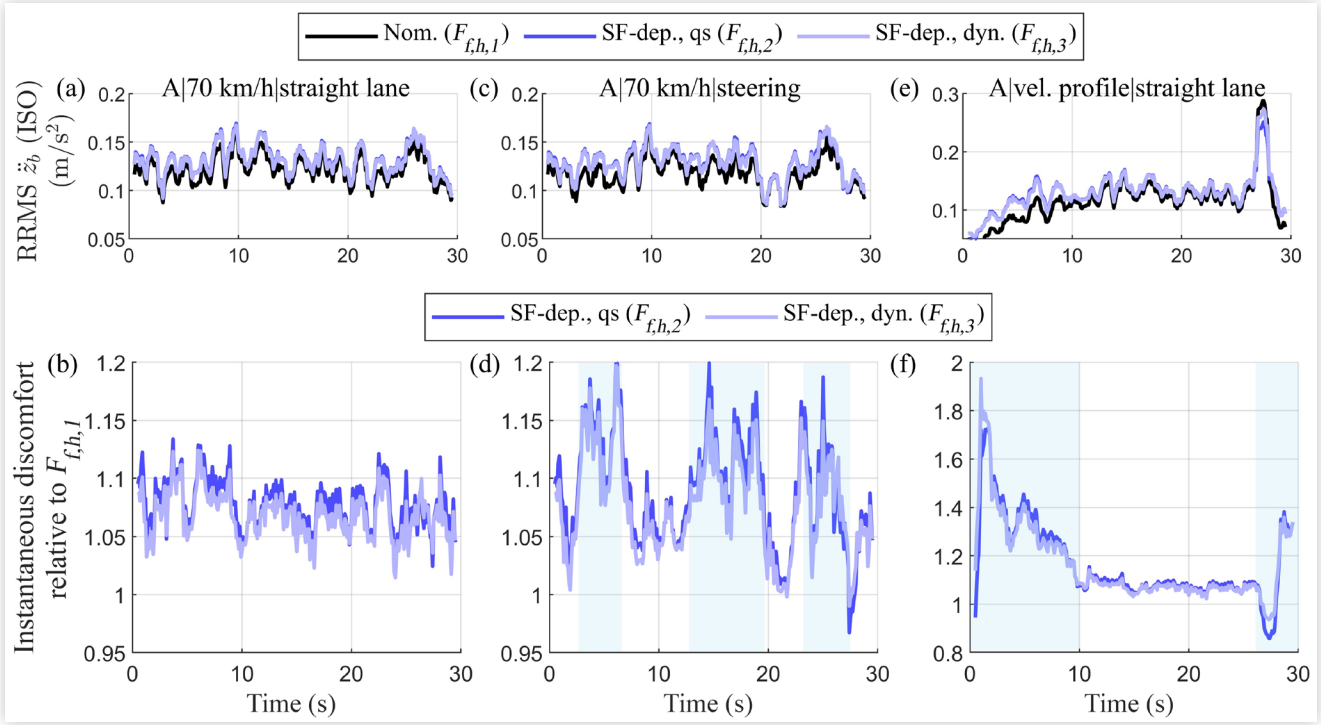
The results of the steering maneuver lead to similar findings. Despite higher horizontal tire forces, average discomfort does not increase substantially compared to straight driving. As discussed in Section 4.2, load transfer limits SF at the inner wheel, while compression reduces friction capacity at the outer wheel, resulting in only moderate increases. Furthermore, there are time segments in which the instantaneous SF falls below the nominal SF present during straight driving. Consequently, average friction capacity remains only slightly elevated relative to straight driving (cf. Table 11), leading to modest discomfort increases at 70 and 100 km/h simulations.

For the straight-lane velocity profile maneuvers (including acceleration, constant driving at 70 km/h, and braking), the average discomfort increases exceed those observed during constant driving at 70 km/h. This is because there are phases of lower speeds, pronouncing the friction effect, and transient high SF levels during acceleration and braking increase the vertical acceleration momentarily. Hence, instantaneous metrics (RRMS) are particularly informative, see Figure 16. Combined steering shows a similar average discomfort increase in analogy to the maneuvers at constant speed.

Roll results are qualitatively similar to vertical acceleration, since roll acceleration is primarily road-introduced. Steering, in contrast, mainly introduces quasi-static roll, while friction effects dominate dynamic behavior. At the 100 km/h maneuvers, the enhanced friction models occasionally reduce roll discomfort, contrary to the general trend. This results from reduced PSD levels in the slip eigenfrequency range, which dominates under ISO weighting for roll (stronger emphasis on lower frequencies).

For the pitch acceleration, the discomfort ratios between the friction models increase for increasing vehicle speed. Pitch behavior is governed by speed-dependent PSD amplification and attenuation. With increasing speed, the first pitch minimum in the PSD is

FIGURE 16 RRMS (a, c, e) and instantaneous discomfort ratio (b, d, f).



© Clemens Deubel, Johannes Meinck, Tobias Schramm, Günther Prokop

shifted toward higher frequencies, see Equation 46. Friction generally increases low-frequency response (in analogy to the vertical acceleration), but ISO frequency weighting for pitch has its maximum close to 1 Hz and decreases thereafter. As vehicle speed decreases, PSD minima shift closer to this peak, reducing weighted pitch acceleration. For the straight-lane velocity profile maneuvers, large pitch accelerations appear during the initialization of acceleration and braking around 1.5 Hz (pitch eigenfrequency), in which the models with higher friction capacity reduce the pitch vibration owing to the damping-like friction effect, thus providing a discomfort ratio <1.

Figure 16 now shows the application of the RRMS method and its characteristics over time. Even under straight driving at constant speed [Figure 16(a)], the RRMS constantly varies due to the stochastic road excitation. Thus, the elevated friction capacities of the enhanced models are momentarily more or less influential [Figure 16(b)], depending on the instantaneous road excitation. The effect of steering (highlighted by the blue boxes) causing increased SF and thus friction capacities, becomes apparent [Figure 16(c) and (d)]. For the velocity profile maneuvers, the segments of acceleration and braking with their corresponding increase in SF and friction capacity can be well observed. The instantaneous discomfort reaches its maximum during these time segments accordingly [Figure 16(e) and (f)].

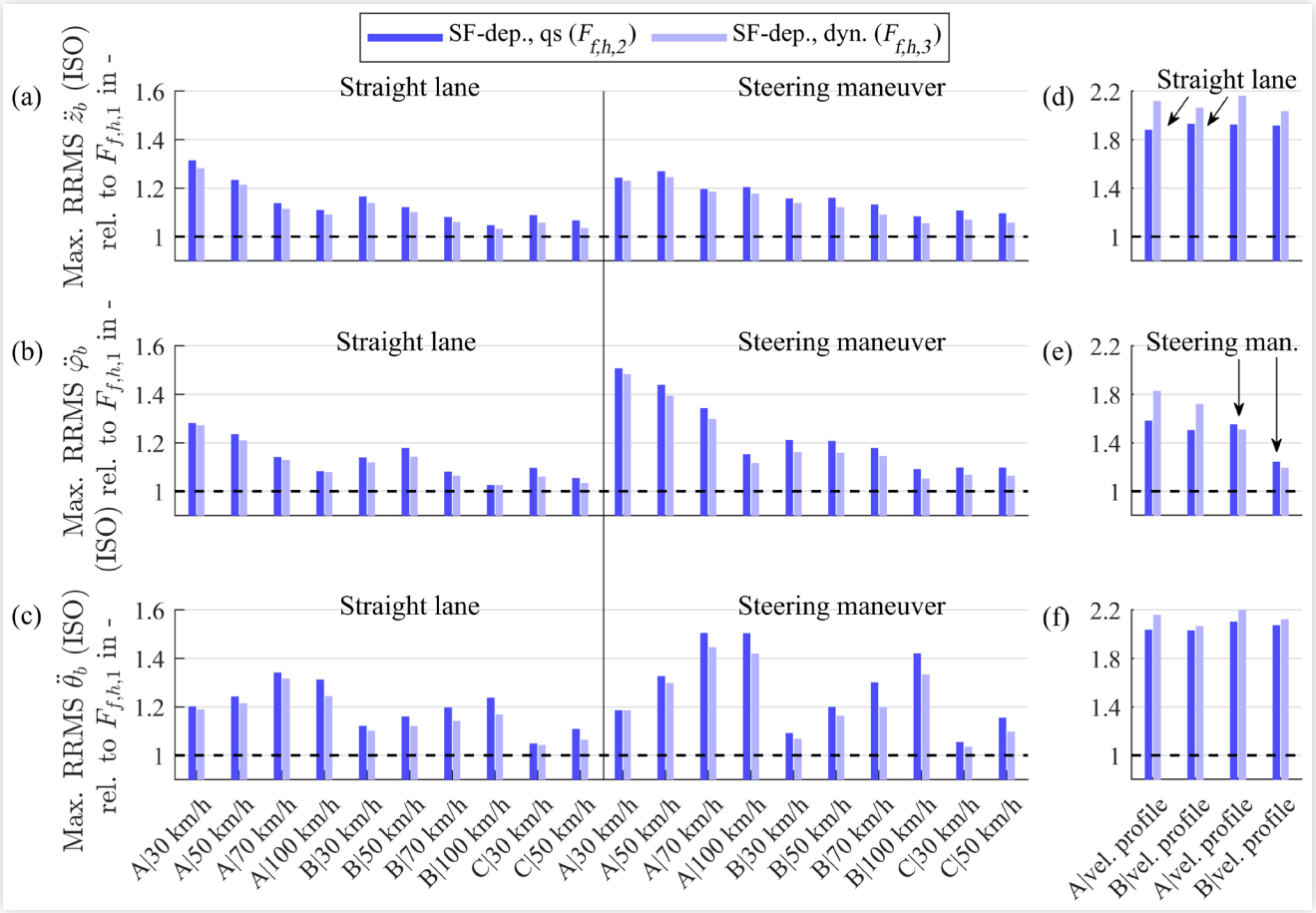
Figure 17 then highlights the maximum instantaneous discomfort ratios across all maneuvers. For straight lane and steering maneuvers, the maximum ratios of the instantaneous discomfort exceed those of the average discomfort, as explained before. For the velocity profile maneuvers, the instantaneous discomfort is far greater than the average discomfort, owing to short but severe transient events. The relative deviations between $F_{f,h,2}$ and $F_{f,h,3}$ are greater when the suspension deflection changes dynamically due to driving maneuvers, reflecting the velocity-dependent dynamic scaling.

4.5. Discussion

The results reveal several general trends regarding the relevance of suspension friction and the required level of friction model complexity. Friction is most influential under mild excitation conditions, i.e., at low vehicle speeds and on high-quality roads. In such cases, hydraulic damping forces remain comparatively small, and friction accounts for a substantial share of the total SA force, cf. Figure I.1.

Across the investigated maneuvers, increasing friction model complexity from $F_{f,h,1}$ to $F_{f,h,3}$ affects the vehicle body response over a wide frequency range. Since friction increases the total SA force, its effect is qualitatively similar to an increase in damping, resulting in a stronger coupling between wheel and body motions. Consequently, the enhanced friction models generally predict higher discomfort levels than the nominal formulation. For low vehicle speeds and smooth road conditions, average

FIGURE 17 Relative RRMS of enhanced friction models to nominal model for vertical body acceleration (a, d), roll acceleration (b, e), and pitch acceleration (c, f).



© Clemens Deubel, Johannes Meinck, Tobias Schramm, Günther Prokop

discomfort increases of approximately 10–15% were observed, while transient acceleration and braking maneuvers may increase instantaneous discomfort by up to approximately 30%. Severe acceleration or braking events amplify instantaneous discomfort further. Similar trends are observed for roll and pitch motion, although vertical acceleration remains the dominant contributor to the weighted discomfort metric.

The simulations further highlight the complex interaction between SF, suspension state, and friction capacity. Stronger cornering does not necessarily increase friction capacity, as the effective SF and the resulting internal normal forces depend on the combined influence of wheel load, tire forces, suspension kinematics, and SA deflection state. Consequently, friction capacity cannot be generalized based on a single vehicle-dynamics quantity, but must be regarded as a coupled suspension system property.

The comparison of the two enhanced friction formulations, $F_{f,h,2}$ and $F_{f,h,3}$, indicates that dynamic friction effects play a secondary role at the vehicle level. Differences between both approaches become noticeable only under highly dynamic excitation, where the velocity-dependent reduction of friction becomes increasingly relevant, particularly at elevated SF levels. However, under these conditions, friction itself becomes less relevant compared to hydraulic damping.

From an application perspective, the principal improvement in modeling accuracy is achieved by accounting for the influence of SF on friction capacity, as implemented already in model $F_{f,h,2}$. Once the modeling framework has been established, implementation of the enhanced formulations is straightforward, and the required parameterization effort remains moderate. Since model $F_{f,h,2}$ requires only quasi-static friction measurements, whereas model $F_{f,h,3}$ additionally requires dynamic parameterization, the quasi-static formulation provides a substantially more favorable balance between modeling effort and accuracy. Therefore, general application of the dynamic formulation cannot be recommended based on the present results.

5. Conclusions

This study investigated the influence of SF-dependent suspension friction modeling on the vertical dynamics of

an MCP suspension vehicle. A modeling framework is developed that determines the instantaneous SA SF from the current kinematic and kinetic suspension state and uses this information to predict friction capacity under realistic driving conditions.

The results demonstrate that suspension friction cannot generally be regarded as capacity-invariant. Instead, friction capacity varies substantially with SF and suspension operating condition, leading to significant effects on vehicle body accelerations and ride comfort–related metrics. Enhanced friction models consistently predict higher discomfort levels than the nominal formulation, with the strongest effects occurring at low vehicle speeds and on smooth roads, where friction contributes significantly to the overall suspension force balance.

Among the investigated approaches, the quasi-static SF-dependent friction model provides the most favorable balance between modeling effort and accuracy. While dynamic friction modeling offers the highest physical fidelity, the additional benefit at the vehicle level remains limited because friction effects become increasingly masked by hydraulic damping as excitation intensity increases.

Overall, the results indicate that SF-dependent friction modeling should be considered whenever high-accuracy ride comfort simulations of MCP suspensions are required. However, the present conclusions are based on a single-vehicle configuration and a comparative simulation framework. While the underlying vehicle model and the newly introduced suspension sub-models are based on established and partially validated modeling approaches, dedicated full-vehicle experiments under identical driving maneuvers are still required to further validate the predicted influence of suspension friction and to assess the transferability of the findings to additional vehicle platforms.

Funding Information

The author(s) received no financial support for the research, authorship, and/or publication of this article.

Declaration of AI-Assisted Technologies

During the preparation of this work, the author(s) used ChatGPT-5.0 in order to check grammar and spelling, as well as to improve the writing style. After using this tool/service, the author(s) reviewed and edited the content as needed and take(s) full responsibility for the content of the published article.

Contact Information

Clemens Deubel, corresponding author
clemens.deubel@tu-dresden.de

CRediT Author Statement

Clemens Deubel: Conceptualization, Data curation, Formal analysis, Investigation, Methodology, Visualization, Writing—original draft, Writing—review and editing

Johannes Meinck: Data curation, Formal analysis, Investigation, Methodology

Tobias Schramm: Software, Writing—review and editing

Günther Prokop: Resources, Supervision

Nomenclature

CoG - Center of gravity
DL - Deflection level
DoF - Degree of freedom
FA - Front axle
FL - Front left (wheel)
FR - Front right (wheel)
HP - Hardpoints
MCP - MacPherson
NRMSE - Normalized root mean squared error
PSD - Power spectral density
RA - Rear axle
RL - Rear left (wheel)
RMS - Root mean square
RMSE - Root mean squared error
RR - Rear right (wheel)
RRMS - Running root mean square
SA - Shock absorber
SF - Side force
TM - Top mount

References

1. Schmidt, H., Büttner, K., and Prokop, G., "Methods for Virtual Validation of Automotive Powertrain Systems in Terms of Vehicle Drivability - A Systematic Literature Review," *IEEE Access* 11 (2023): 27043-27065, doi:https://doi.org/10.1109/ACCESS.2023.3257106.

2. Stretz, A., "Komfortrelevante Wechselwirkung von Fahrzeugschwingungsdämpfern und den elastischen Dämpferlagern [Comfort Relevant Interrelations of Vehicle Shock Absorbers and Elastic Shock Absorber Bushings—in German]," PhD thesis, Technische Universität Darmstadt, Darmstadt, Germany, 2011.
3. Dessort, R., Meissner, M., Kolmeder, S., Prokop, G. et al., "Experimental Nonlinear System Identification of a Shock Absorber Focusing on Secondary Ride Comfort," in Pfeffer, P., ed., *12th International Munich Chassis Symposium 2021* (Munich: Springer-Verlag GmbH Germany, 2022), 218-40, doi:https://doi.org/10.1007/978-3-662-64550-5_13.
4. Barethiye, V., Pohit, G., and Mitra, A., "A Combined Nonlinear and Hysteresis Model of Shock Absorber for Quarter Car Simulation on the Basis of Experimental Data," *Eng Sci Technol Int J* 20 (2017): 1610-1622, doi:https://doi.org/10.1016/j.jestch.2017.12.003.
5. Pellegrini, E., Koch, G., Spirk, S., and Lohmann, B., "A Dynamic Feedforward Control Approach for a Semi-Active Damper Based on a New Hysteresis Model," *Proceedings of the 18th IFAC World Congress, IFAC 2011*, Milan, Italy, 2011, 6248-53, https://doi.org/10.3182/20110828-6-IT-1002.02914.
6. Zauner, C., Edelmann, J., and Plöchl, M., "Modelling, Validation and Characterisation of High-Performance Suspensions by Means of a Suspension Test Rig," *Int J Veh Des* 79 (2019): 107-126, doi:https://doi.org/10.1504/IJVD.2019.102333.
7. Besinger, F.H., Cebon, D., and Cole, D.J., "Damper Models for Heavy Vehicle Ride Dynamics," *Veh Syst Dyn* 24 (1995): 35-64, doi:https://doi.org/10.1080/00423119508969081.
8. Herzog, L., "Theoretical and Experimental Investigations of the Friction Behavior of Automotive Shock Absorbers," PhD thesis, Technische Universität Ilmenau, Ilmenau, Germany, 2021, https://doi.org/10.22032/dbt.50596.
9. Lizarraga, J., Sala, J.A., and Biera, J., "Modelling of Friction Phenomena in Sliding Conditions in Suspension Shock Absorbers," *Veh Syst Dyn* 46, no. S1 (2008): 751-764, doi:https://doi.org/10.1080/00423110802037024.
10. Kumar, M.S. and Vijayarangan, S., "Analytical and Experimental Studies on Active Suspension System of Light Passenger Vehicle to Improve Ride Comfort," *Mechanika* 65 (2007): 34-41, doi:https://doi.org/10.5755/j02.mech.14828.
11. Mántaras, D.A. and Luque, P., "Ride Comfort Performance of Different Active Suspension Systems," *Int J Veh Des* 40 (2006): 106-125, doi:https://doi.org/10.1504/IJVD.2006.008456.
12. León-Vargas, F., Garelli, F., and Zapateiro, M., "Limiting Vertical Acceleration for Ride Comfort in Active Suspension Systems," *Proc Inst Mech Eng Part I: J Syst Control Eng* 232 (2018): 223-232, doi:https://doi.org/10.1177/0959651817745469.
13. Munawwarah, S. and Yakub, F., "Control Analysis of Vehicle Ride Comfort through Integrated Control Devices on the Quarter and Half Car Active Suspension Systems," *Proc Inst Mech Eng Part D: J Automob Eng* 235 (2021): 1256-1268, doi:https://doi.org/10.1177/0954407020968300.
14. Komori, K., Fujimoto, G., Tsukamoto, T., and Endo, D., "Effect of Friction Reduction of Magneto-Rheological Semi-Active Damper on Ride Comfort and Vehicle Dynamics," *8th International Munich Chassis Symposium 2017*, Munich, 2017, 309-29, https://doi.org/10.1007/978-3-658-18459-9_26.
15. Deubel, C. and Prokop, G., "The Relevance of Shock Absorber Friction on the Total Friction of a MacPherson Suspension System during Lateral Manoeuvres," *Proc Inst Mech Eng Part D: J Automob Eng* 239 (2024): 6679-6696, doi:https://doi.org/10.1177/09544070241289270.
16. Hastey, J., Jacques, B., Eric, G., Colin, J. et al., "Optimization on Mac Pherson Suspensions with a Spring," *SAE International Congress and Exposition*, Detroit, Michigan, United States, February 24, 1997, https://doi.org/10.4271/970100.
17. Hamano, T., Nakamura, T., Enomoto, H., Sato, N. et al., "Development of L-Shape Coil Spring to Reduce a Friction on the McPherson Strut Suspension System," *SAE 2001 World Congress*, Detroit, Michigan, United States, March 5, 2001, https://doi.org/10.4271/2001-01-0497.
18. Wünsche, T., Muhr, K., Biecker, K., and Schnaubelt, L., "Side Load Springs as a Solution to Minimize Adverse Side Loads Acting on the McPherson Strut," *International Congress & Exposition*, Detroit, Michigan, United States, February 28, 1994, https://doi.org/10.4271/940862.
19. Dahl, P.R., "A Solid Friction Model," TOR-0158, The Aerospace Corporation, El Segundo, CA, 1968.
20. Xuwang, W., Chen, X., Xu, P., and Zhang, Y., "The Effect of Friction on Ride Comfort Simulation and Suspension Optimization," *WCX SAE World Congress Experience*, Detroit, Michigan, United States, April 21, 2020, https://doi.org/10.4271/2020-01-0765.
21. Yabuta, K., Hidaka, K., and Fukushima, N., "Effects of Suspension Friction on Vehicle Riding Comfort," *Veh Syst Dyn* 10 (1981): 85-91, doi:https://doi.org/10.1080/00423118108968641.
22. Benini, C., Gadola, M., Chindamo, D., Uberti, S. et al., "The Influence of Suspension Components Friction on Race Car Vertical Dynamics," *Veh Syst Dyn* 55 (2017): 338-350, doi:https://doi.org/10.1080/00423114.2016.1267370.
23. Angrick, C., Prokop, G., Knauer, P., and Wagner, A., "Improved Prediction of Ride Comfort Characteristics by Considering Suspension Friction in the Automotive Development Process," in Pfeffer, P., ed., *6th International Munich Chassis Symposium* (Munich: Springer Vieweg Wiesbaden, 2015), 377-403, doi:https://doi.org/10.1007/978-3-658-09711-0_25.
24. Schramm, T., Deubel, C., and Prokop, G., "A Suspension Friction Model to Investigate the Influence of Degraded

Shock Absorbers on Vehicle Dynamics," *Proc Inst Mech Eng Part D: J Automob Eng* 240, no. 9 (2026): 6104-6117, doi:https://doi.org/10.1177/09544070251381918.

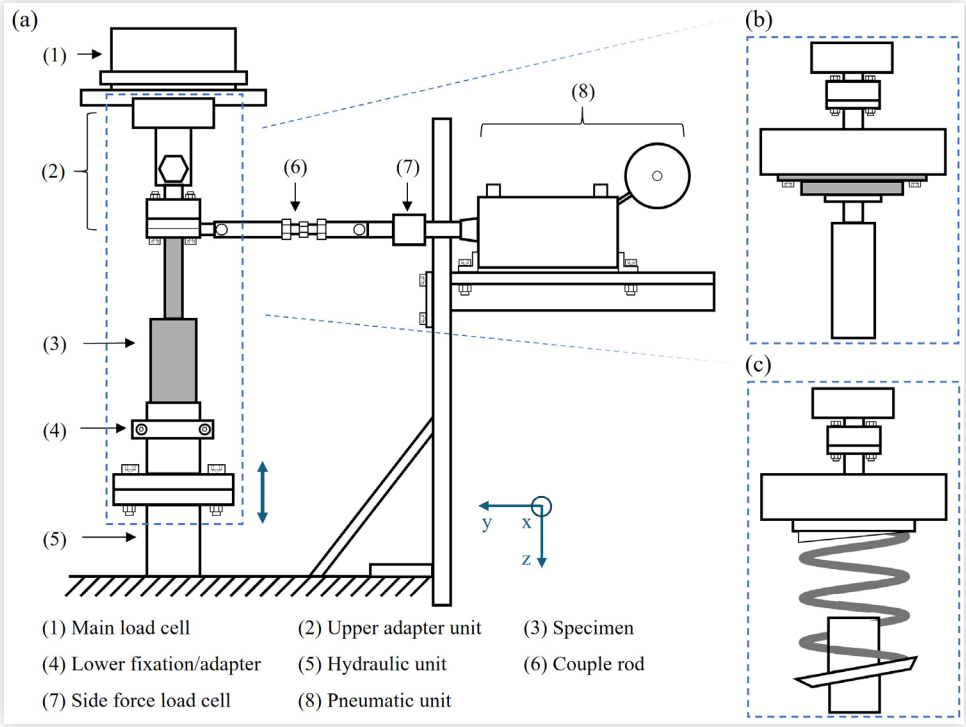
25. Deubel, C., Dittrich, B., Meinck, J., and Prokop, G., "Experimental Analysis and Modelling of Friction in Automotive Shock Absorbers Operating under Side Forces," *Tribol Int* 215 (2025): 111328, doi:https://doi.org/10.1016/j.triboint.2025.111328.
26. Deubel, C., Schneider, S., and Prokop, G., "Effect of Shock Absorber Friction on Vehicle Vertical Dynamics," *SAE Int. J. Veh. Dyn., Stab., and NVH* 8, no. 2 (2024): 155-177, doi:https://doi.org/10.4271/10-08-02-0010.
27. Alonso, M. and Comas, A., "Modelling a Twin Tube Cavitating Shock Absorber," *Proc Inst Mech Eng Part D: J Automob Eng* 220 (2006): 1031-1040, doi:https://doi.org/10.1243/09544070D23104.
28. Canudas de Wit, C., Olsson, H., Aström, K.J., and Lischinsky, P., "A New Model for Control of Systems with Friction," *IEEE Trans Automat Contr* 40 (1995): 419-425, doi:https://doi.org/10.1109/9.376053.
29. Lohse, C., "Über Wechselwirkungen in Elastomerlagern und deren Einfluss auf die Elastokinematik einer Vorderradaufhängung [About Interrelations in Elastomer Bushings and Their Influence on the Elastokinematics of a Front Suspension—in German]," PhD thesis, Technische Universität Bergakademie Freiberg, Freiberg, Germany, 2016.
30. Berg, M., "A Nonlinear Rubber Spring Model for Vehicle Dynamics Analysis," *Veh Syst Dyn* 29 (1998): 723-728, doi:https://doi.org/10.1080/00423119808969599.
31. Sjöberg, M., "Rubber Isolators – Measurements and Modelling Using Fractional Derivatives and Friction," *International Truck & Bus Meeting & Exposition*, Portland, Oregon, United States, December 4, 2000, https://doi.org/10.4271/2000-01-3518.
32. Gotoh, T. and Imaizumi, T., "Optimization of Force Action Line with New Spring Design on the MacPherson Strut Suspension for Riding Comfort," *SAE 2000 World Congress* Detroit, Michigan, United States, March 6, 2000, https://doi.org/10.4271/2000-01-0101.
33. Liu, J., Zhuang, D.J., Yu, F., and Lou, L.M., "Optimized Design for a MacPherson Strut Suspension with Side Load Springs," *Int J Automot Technol* 9 (2008): 29-35, doi:https://doi.org/10.1007/s12239-008-0004-y.
34. Löhe, K., "Ein modellgestütztes Konzept zur fahrbahnadaptiven Fahrwerksregelung [A Model-Based Concept for Road-Adaptive Suspension Control—in German]," PhD thesis, Friedrich-Alexander-Universität Erlangen-Nürnberg, Erlangen, Germany, 2018, https://doi.org/10.25593/978-3-96147-102-7.
35. ISO 8608, "Mechanical Vibration—Road Surface Profiles—Reporting of Measured Data 2016, 2nd ed.
36. Schmeitz, A.J.C., "A Semi-Empirical Three-Dimensional Model of the Pneumatic Tyre Rolling over Arbitrarily Uneven Road Surfaces," PhD thesis, Technische Universität Delft, Delft, the Netherlands, 2004.
37. Rostami, H.T., Najafabadi, M.F., and Ganji, D.D., "Investigation of Tire Stiffness and Damping Coefficients Effects on Automobile Suspension System," *Proc Inst Mech Eng Part D: J Automob Eng* 237, no. 14 (2023): 3313-3325, doi:https://doi.org/10.1177/09544070231151860.
38. Deubel, C., Meinck, J., and Prokop, G., "Ride Comfort Assessment Considering the Effect of Shock Absorber Friction Influenced by Horizontal Tire Forces," *2025 FISITA World Mobility Conference Technical Proceedings: Volume 1*, Barcelona, 2026, Springer, doi: https://doi.org/10.1007/978-3-032-13861-3_2.
39. Butcher, J.C., *Numerical Methods for Ordinary Differential Equations Numerical Methods for Ordinary Differential Equations* (Chichester, United Kingdom: John Wiley & Sons, 2016), doi:https://doi.org/10.1002/9781119121534.
40. Duda, R.O., Hart, P.E., and Stork, D.G., *Pattern classification*, 2nd ed. (New York: John Wiley & Sons, 2001).
41. Mitschke M., Wallentowitz H.. *Dynamik der Kraftfahrzeuge [Dynamics of Road Vehicles]*—Book in German, 5th ed. (Wiesbaden: Springer Vieweg, 2014), doi:https://doi.org/10.1007/978-3-658-05068-9.
42. Koletzko, C., "Untersuchung des Einflusses von Verstelldämpfern auf das Wankverhalten von PKW unter Berücksichtigung einer aktiven Wankstabilisierung [Investigation of the Influence of Adjustable Dampers on the Roll Behaviour of Passenger Cars...]," PhD thesis, Technische Universität München, Munich, Germany, 2008.
43. Bellem, H., Thiel, B., Schrauf, M., and Krems, J.F., "Comfort in Automated Driving: An Analysis of Preferences for Different Automated Driving Styles and Their Dependence on Personality Traits," *Transp Res Part F* 55 (2018): 90-100, doi:https://doi.org/10.1016/j.trf.2018.02.036.
44. Bubb, H., "Komfort und Diskomfort: Definition und Überblick [Comfort and Discomfort: Definition and Overview - Article in German]," *Ergon Aktuell - Tech Univ München* 3 (2003): 5-8.
45. Aledhari, M., Member, S., Rahouti, M., Qadir, J. et al., "Motion Comfort Optimization for Autonomous Vehicles: Concepts, Methods, and Techniques," *IEEE Internet Things J* 11 (2024): 378-402, doi:https://doi.org/10.1109/JIOT.2023.3287489.
46. Domova, V., Currano, R.M., and Sirkin, D., "Comfort in Automated Driving: A Literature Survey and a High-Level Integrative Framework," *Proc ACM Interactive, Mobile, Wearable Ubiquitous Technol* 8 (2024): 1-23, doi:https://doi.org/10.1145/3678583.
47. Elbanhawi, M., Simic, M., and Jazar, R., "In the Passenger Seat: Investigating Ride Comfort Measures in Autonomous Cars," *IEEE Intell Transp Syst Mag* 7 (2015): 4-17, doi:https://doi.org/10.1109/MITS.2015.2405571.
48. ISO 2631-1, "Mechanical Vibration and Shock - Evaluation of Human Exposure to Whole-Body Vibration 2003," 2003, 13.

49. Griffin, M.J., "Frequency-dependence of Psychophysical and Physiological Responses to Hand-transmitted Vibration," *Ind Health* 50 (2012): 354-369, doi:https://doi.org/10.2486/indhealth.ms1379.
50. Dupuis, H. and Zerlett, G., "Beanspruchung des Menschen durch mechanische Schwingungen: Kenntnisstand zur Wirkung von Ganz-Körper-Schwingungen [Human Exposure to Mechanical Vibrations: State of Knowledge on the Effect of Whole-Body Vibrations—Report in German]," Schriftenreihe des Hauptverbandes der Gewerblichen Berufsgenossenschaften e.V., Bonn, 1984.
51. Barbu, D.M., "Modeling of the Seated Human Body in a Vibrational Medium," *Appl. Mech. Mater.* 658 (2014): 401-406, doi:https://doi.org/10.4028/www.scientific.net/AMM.658.401.

Appendices

Appendix A: Test Rig, SA Test Program and SA Specimen

FIGURE A.1 One-axis hydropulser with shock absorber (a), top mount (b), and spring (c).



© Clemens Deubel, Johannes Meinck, Tobias Schramm, Günther Prokop

TABLE A.1 Test rig information.

Characteristics	Specification
Manufacturer	MTS Systems Corporation
Maximum stroke	250 mm
Maximum velocity	2 m/s
Maximum dynamics	100 Hz at 0.5 mm
Maximum load	50 kN in the vertical axis
Side force application	In one axis perpendicular to main excitation axis; by pneumatic actuator; max force 6 kN
Specimen	Shock absorber, strut, spring, tire, bushing

© Clemens Deubel, Johannes Meinck, Tobias Schramm, Günther Prokop

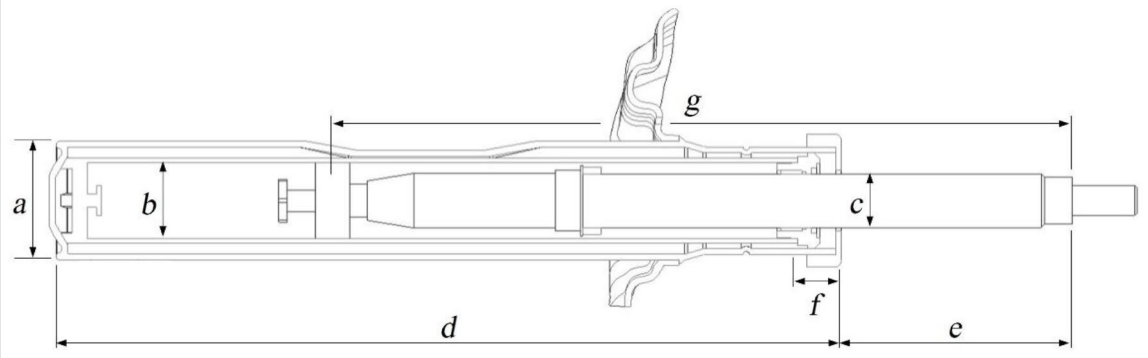
TABLE A.2 Test program for parameterization and validation of the SA.

TP	Component/property	Test configuration and varied parameters: Excitation/amplitude/velocity (frequency)/no. of periods (duration)/repetitions/further specification	Parameterization/validation
1	SA/gas stiffness	• Triangular/25 mm/0.5 mm · s^{-1}/3 periods/1 rep.	Parameterization
2	SA/steady-state hydraulic damping curve	• Sine/25 mm/0.5–1000 mm · s^{-1}/3–10 periods/1 rep. • Sine sweep/4 mm/0.1–25 Hz/45 s/5 rep. • Sine sweep/10 mm/0.1–15 Hz/45 s/5 rep.	Parameterization
3	SA/Pellegrini param. (hydraulic damping)	• Red noise/32 mm (max)/0.2–30 Hz/45 s/10 rep.	Parameterization
4		• Sine sweep/30–0.5 mm log. ↓/0.1–25 Hz/45 s/5 rep. • Recorded SA travel profile/-/-/60 s/10 rep.	Validation
5	SA/quasi-static friction parameters	• Triangular/3 mm/0.5 mm · s^{-1}/10 periods/2 rep. Each DL = $K0_{SA}$ {−20 − 10 0 + 10 + 20} mm	Parameterization
6	SA/total SA force under SF	• Sine/10 mm/5 | 50 | 100 | 150 mm · s^{-1}/10 periods/5 rep./SF changing over periods • SA displ. profile class A/max. ≈ 2 mm/max. ≈ 44 mm · s^{-1}/60 s/10 rep/SF changing over time • SA displ. profile class B/max. ≈ 15 mm/max. ≈ 328 mm · s^{-1}/60 s/10 rep/SF changing over time	Validation

© Clemens Deubel, Johannes Meinck, Tobias Schramm, Günther Prokop

TABLE A.3 Dimensions of SA specimen.

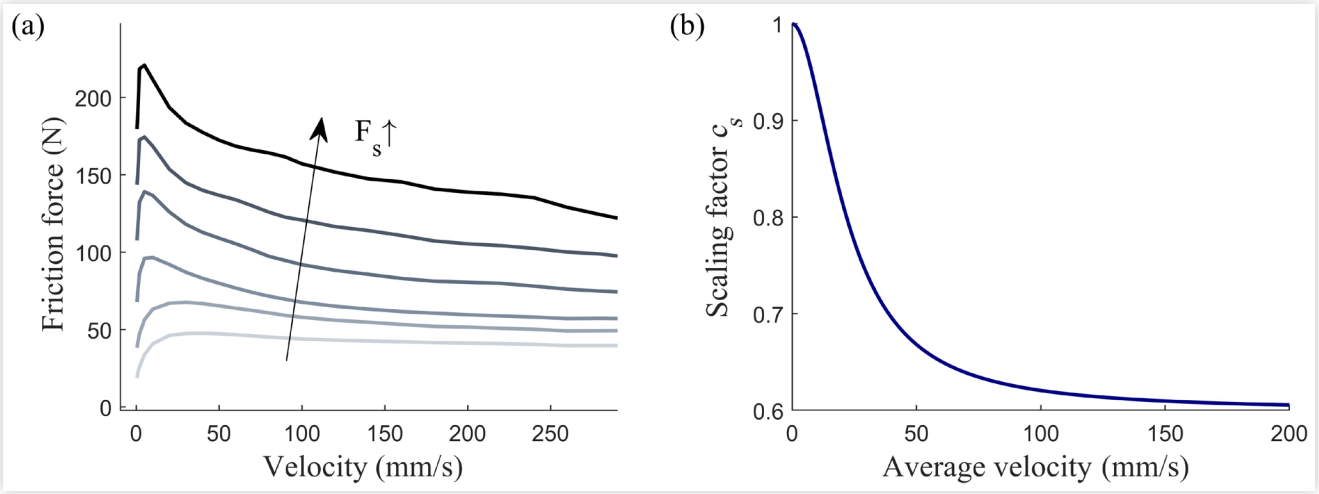
Dimension	Value (mm)	Dimension	Value (mm)
a (tube diameter)	50.0	*e* (free piston rod length)	118.0
b (inner cylinder diameter)	35.0	*f* (distance to rod guide)	15.0
c (piston rid diameter)	25.0	*g* (total piston rod length)	250.0
d (tube height)	326.0		



© Clemens Deubel, Johannes Meinck, Tobias Schramm, Günther Prokop

Appendix B: Steady-State Friction Curves and Scaling Factor

FIGURE B.1 Steady-state friction curves (a) and scaling factor (b).



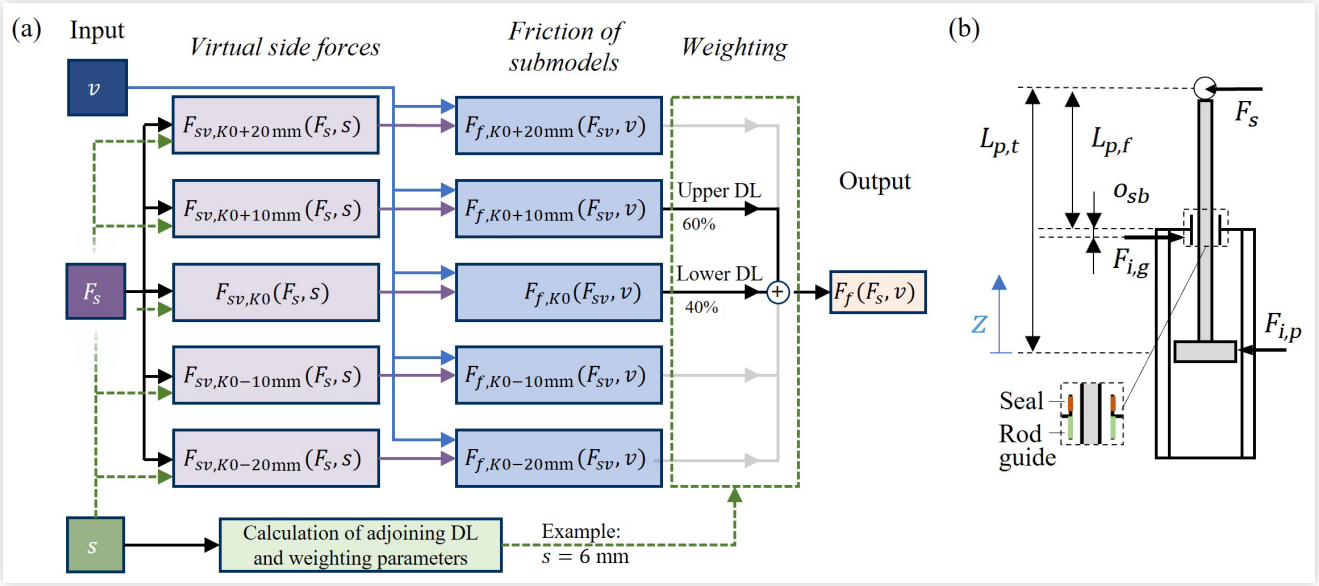
© Clemens Deubel, Johannes Meinck, Tobias Schramm, Günther Prokop

Appendix C: Procedure for Considering the Interrelation of SA Friction and Deflection State

During each time step of the simulation, information on the current deflection level (DL) and the experimentally investigated DLs are combined in the following approach, which is shown in Figure C.1(a):

1. The Dahl parameters are defined according to SF following Equations 16 and 17 for the investigated DLs.
2. For the same DLs, the friction force is calculated individually depending on the SF using the respective parameters. In this case, there are five friction sub-models corresponding to the five DLs experimentally investigated.

FIGURE C.1 Workflow to consider deflection level (a) and overview of inner normal SA forces (b).



© Clemens Deubel, Johannes Meinck, Tobias Schramm, Günther Prokop

3. The two DLs adjacent to the current value of the instantaneous deflection are identified.
4. Their respective friction forces are linearly weighted according to the instantaneous deflection and superimposed to obtain the total friction force.

Since the instantaneous deflection may exceed the experimentally parameterized range, extrapolation is required. This is achieved by considering the internal SA normal forces, see Figure C.1(b), which are functions of SF and the geometric properties.

First, the internal normal forces at the two relevant SA contact interfaces, rod guidance–piston rod $F_{i,g}$ and piston–cylinder $F_{i,p}$ can be derived from the inner geometry. Note that there is also friction arising from the seal–rod interaction, which is, however, independent of SF and therefore not further considered here. With $L_{p,t}$ denoting the total piston rod length, $L_{p,f}$ the free piston rod length, o_{sb} the distance of the upper tube end to the piston rod guide, and z the current deflection relative to $K0$, it follows:

$$F_{i,g}\left(F_s,z\right) = F_s \cdot \frac{L_{p,t}}{L_{p,t} - L_{p,f} - o_{sb} - z}$$

$$F_{i,p}\left(F_s,z\right) = F_s \cdot \frac{L_{p,f} + o_{sb} + z}{L_{p,t} - L_{p,f} - o_{sb} - z}$$

Both normal forces increase linearly with the applied SF. From purely geometric considerations, it is already evident that the rod guide contact carries substantially higher loads than the piston–cylinder interface, since $L_{p,t} \approx 2.5...3 \cdot L_{p,f}$. The friction coefficients $\mu_{i,g}$, $\mu_{i,g'}$, $\mu_{i,p}$, $\mu_{i,p'}$ are identified using a least-squares parameter estimation approach. The resulting friction force, derived from the estimated coefficients, exhibits a quadratic dependence on SF:

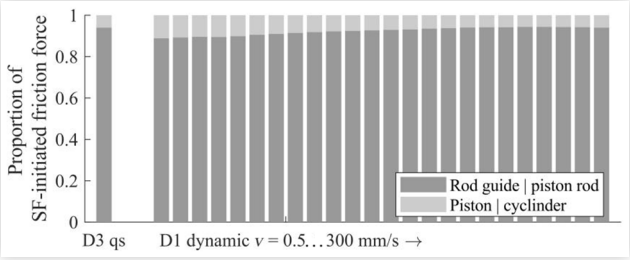
$$F_{f,calc} = F_{f,const} + F_{i,g} \cdot \left(\mu_{i,g} + \mu_{i,g'} \cdot F_{i,g}\right) + F_{i,p} \cdot \left(\mu_{i,c} + \mu_{i,c'} \cdot F_{i,p}\right)$$

The estimation method aims to minimize the error E_j between experimental $F_{f,exp}$ and calculated friction force for each SF j, resulting in an ideal parameter set:

$$\sum_{j=1}^{n}\left[F_{i,b} \cdot \left(\mu_{i,g} + \mu_{i,g'} \cdot F_{i,g}\right) + F_{i,p} \cdot \left(\mu_{i,p} + \mu_{i,p'} \cdot F_{i,p}\right) - \left(F_{f,exp} - F_{f,const}\right)\right]^2 \rightarrow \min$$

In turn, the individual friction force contributions can be determined. It is evident that both, in the quasi-static domain for SA "Pas-3" and in the quasi-static plus dynamic domain for SA "Pas-1," the contact rod guide–piston rod accounts for approx. 90% of the SF-initiated friction force.

FIGURE C.2 Proportion of SF-initiated friction force depending on SA velocity.



© Clemens Deubel, Johannes Meinck, Tobias Schramm, Günther Prokop

Given the linear relationship between SF and individual normal forces, as well as the primarily (not exactly) linear increase of friction per SF, changes in normal force during compression or rebound can be used to approximate the corresponding change in friction. Consequently, a virtual SF F_{sv} is introduced to represent the variation in internal normal forces. This virtual SF is obtained by relating the normal forces at the current deflection z to those at a reference deflection z_{ref} (which marks one of the five experimentally investigated DLs):

$$F_{sv} = 0.9 \cdot F_s \cdot \frac{F_{i,g}\left(F_s,z\right)}{F_{i,g}\left(F_s,z_{ref}\right)} + 0.1 \cdot F_s \cdot \frac{F_{i,p}\left(F_s,z\right)}{F_{i,p}\left(F_s,z_{ref}\right)}$$

In summary, approx. 90% of total SA friction originates from the piston rod guide and about 10% from the piston–cylinder contact, rendering the latter secondary. Because both the internal normal forces and friction force, scale approximately linearly with SF, a virtual SF F_{sv} is introduced to account for deflection-induced changes in normal force.

$$F_{sv}\left(F_s,z\right) = F_{sv} = 0.9 \cdot F_s \cdot \frac{F_{i,g}\left(F_s,z\right)}{F_{i,g}\left(F_s,z_{ref}\right)} + 0.1 \cdot F_s \cdot \frac{F_{i,p}\left(F_s,z\right)}{F_{i,p}\left(F_s,z_{ref}\right)}$$

For example, when the instantaneous deflection z reaches $z > z_{ref} = K0_{SA}$+ 20 mm, there is $F_{sv} > F_s$, resulting in higher friction forces calculated by the model. This approach allows calculating the friction force realistically for any excitation. This step is situated before step (1) of the outlined process. However, it is obvious that the farther the instantaneous deflection lies outside the parameterized range, the greater the inaccuracy becomes. The model variants 2 and 3 make use of this workflow.

Appendix D: Test Program, Parameterisation and Validation Results of the TM

TABLE D.1 Test program for parameterization and validation of the TM.

© Clemens Deubel, Johannes Meinck, Tobias Schramm, Günther Prokop

TP	Component/property	Test configuration and varied parameters: excitation/ amplitude/velocity (frequency)/no. of periods (duration)/repetitions/further specification	Parameterization/validation
1	Coil spring path stiffness	• Triangular/8 kN/50 N · s^{-1}/3 periods/1 rep. • Triangular/0.2 mm/1–25 Hz/20 periods/1 rep.	Parameterization
2	SA path stiffness and friction parameters	• Red noise/2.2 mm (max)/0.2–30 Hz/45 s/10 rep. • Sine sweep/0.5 mm/0.1–25 Hz/45 s/10 rep. • Sine/0.2 | 0.5 mm/10 | 15 | 20 Hz/10 periods/1 rep.	Parameterization
		• Sine sweep/0.2 mm/0.1–25 Hz/45 s/10 rep. • Sine sweep/1.0 mm/0.1–25 Hz/45 s/10 rep. • Recorded TM travel profile/-/-/120 s/10 rep.	Validation

TABLE D.2 Parameters of the TM SA path model.

Parameter	Value	Unit
$k_{TM,SA,1}$	689,140	N/m
$k_{TM,SA,2}$	$-9.01 \cdot 10^{6}$	N/m^2
$k_{TM,SA,3}$	$-4.14 \cdot 10^{10}$	N/m^3
$k_{TM,SA,4}$	$-1.10 \cdot 10^{12}$	N/m^4
$k_{TM,SA,5}$	$9.57 \cdot 10^{15}$	N/m^5
$F_{TM,SA,f,max}$	69.2	N
x_2	$1.45 \cdot 10^{-4}$	m

© Clemens Deubel, Johannes Meinck, Tobias Schramm, Günther Prokop

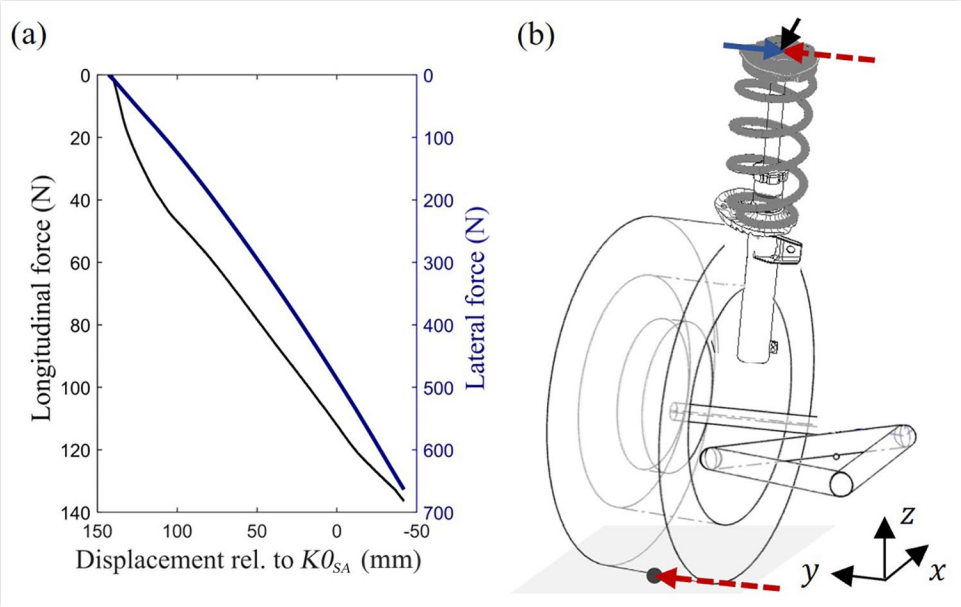
TABLE D.3 Results of parameterization and validation of the TM SA path model.

© Clemens Deubel, Johannes Meinck, Tobias Schramm, Günther Prokop

Excitation signal	RMSE (N)	NRMSE (%)
Parameterization		
Sine 0.2 mm 10 Hz	3.3	3.0
Sine 0.2 mm 15 Hz	3.3	3.2
Sine 0.2 mm 20 Hz	3.1	3.4
Sine 0.5 mm 10 Hz	8.5	3.3
Sine 0.5 mm 15 Hz	9.1	3.8
Sine 0.5 mm 20 Hz	9.4	4.2
Sine sweep 0.5 mm	6.9	2.8
Red noise	15.9	3.2
Validation		
Sine sweep 0.2 mm	5.4	5.3
Sine sweep 1.0 mm	8.8	1.9
TM displ. profile	27.4	7.3

Appendix E: Coil Spring Forces

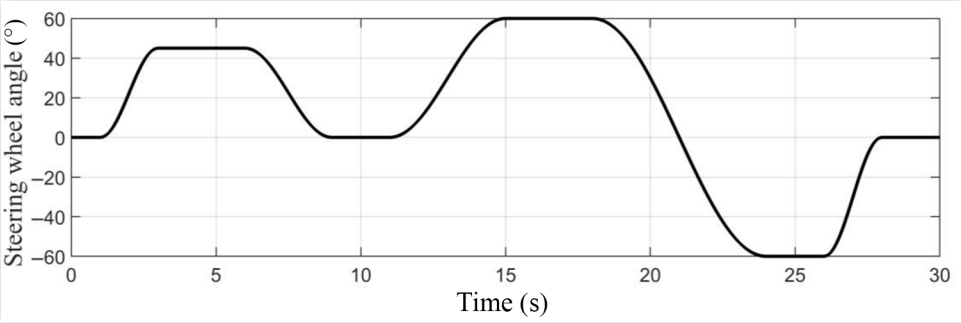
FIGURE E.1 Coil spring forces (a) and visualization in suspension (b).



© Clemens Deubel, Johannes Meinck, Tobias Schramm, Günther Prokop

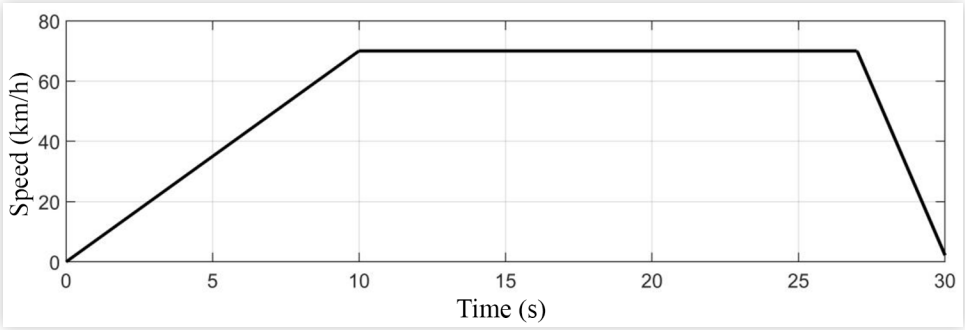
Appendix F: Additional Input Profiles for Full-Vehicle Simulation

FIGURE F.1 Steering wheel angle profile for full-vehicle simulation.



© Clemens Deubel, Johannes Meinck, Tobias Schramm, Günther Prokop

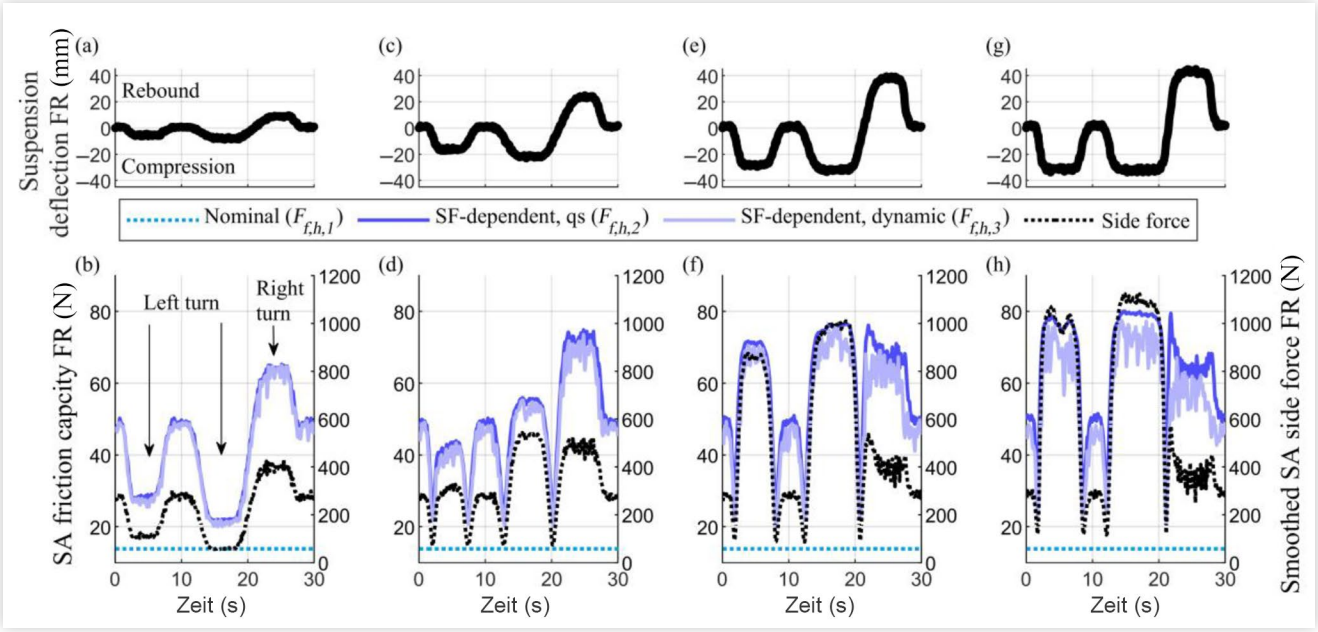
FIGURE F.2 Vehicle speed target profile for full-vehicle simulation.



© Clemens Deubel, Johannes Meinck, Tobias Schramm, Günther Prokop

Appendix G: SA Side Force, Friction Capacity and Suspension Deflection of FR

FIGURE G.1 FR: SA side force and friction capacity (lower row) plus suspension deflection (upper row) during acceleration (a–d), and during combined acceleration and steering (e–h).



© Clemens Deubel, Johannes Meinck, Tobias Schramm, Günther Prokop

Appendix H: Objective Ride Comfort Values

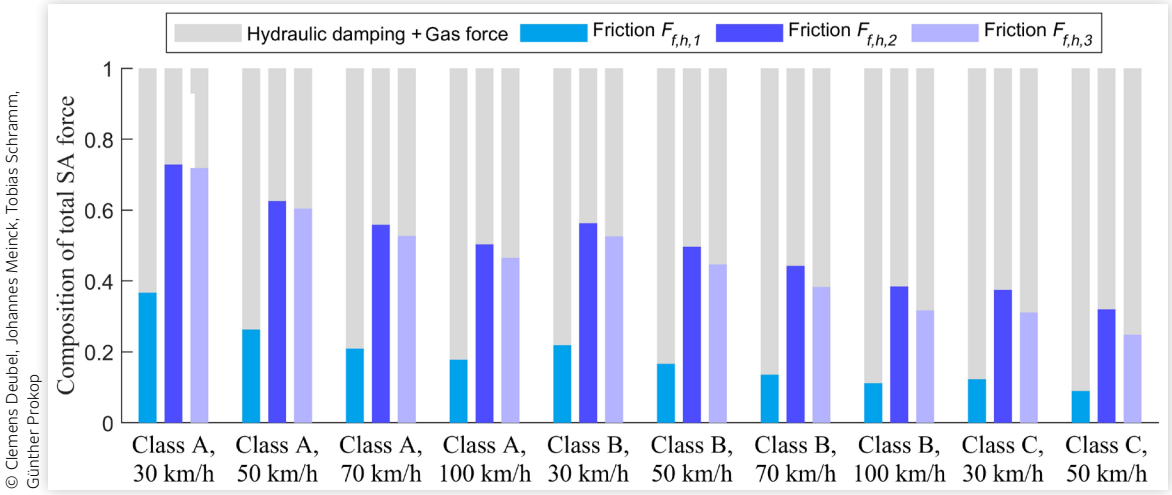
TABLE H.1 Summary of objective ride comfort values depending on maneuver and suspension friction modeling.

Maneuver	RMS			RMS relative to $F_{f,h,1}$ (mean discomfort ratio)						Maximum RRMS relative to $Ff_{,}h_{,1}$ (maximum instantaneous discomfort ratio)					
	m/s²	°/s²	°/s²												
Road | vel. | steering	$\ddot{z}_b$	$\ddot{\varphi}_b$	$\ddot{\theta}_b$	$\ddot{z}_b$		$\ddot{\varphi}_b$		$\ddot{\theta}_b$		$\ddot{z}_b$		$\ddot{\varphi}_b$		$\ddot{\theta}_b$	
		$F_{f,h,1}$		$F_{f,h,2}$	$F_{f,h,3}$	$F_{f,h,2}$	$F_{f,h,3}$	$F_{f,h,2}$	$Ff_{,}h_{,3}$	$F_{f,h,2}$	$F_{f,h,3}$	$F_{f,h,2}$	$F_{f,h,3}$	$F_{f,h,2}$	$F_{f,h,3}$
A | 30 km/h | none	0.08	2.36	0.943	1.18	1.16	1.10	1.09	1.02	1.02	1.32	1.28	1.28	1.27	1.20	1.19
A | 50 km/h | none	0.10	2.68	1.104	1.15	1.13	1.11	1.10	1.15	1.12	1.23	1.21	1.24	1.21	1.24	1.22
A | 70 km/h | none	0.11	2.92	1.095	1.08	1.07	1.01	1.01	1.19	1.16	1.14	1.12	1.14	1.13	1.34	1.32
A | 100 km/h | none	0.12	3.78	1.033	1.04	1.03	0.97	0.98	1.19	1.15	1.11	1.09	1.08	1.08	1.31	1.24
B | 30 km/h | none	0.13	4.38	1.760	1.10	1.07	1.04	1.03	1.00	1.00	1.17	1.14	1.14	1.12	1.12	1.10
B | 50 km/h | none	0.18	4.55	1.885	1.07	1.05	1.06	1.04	1.09	1.06	1.12	1.10	1.18	1.14	1.16	1.12
B | 70 km/h | none	0.20	5.55	1.802	1.05	1.03	0.99	1.00	1.10	1.07	1.08	1.06	1.08	1.06	1.20	1.14
B | 100 km/h | none	0.22	7.88	1.709	1.02	1.02	0.98	0.98	1.10	1.06	1.05	1.03	1.03	1.03	1.24	1.17
C | 30 km/h | none	0.24	7.53	3.516	1.05	1.03	1.01	1.00	1.00	1.00	1.09	1.06	1.10	1.06	1.05	1.04
C | 50 km/h | none	0.31	8.18	3.660	1.04	1.02	1.01	1.00	1.04	1.02	1.07	1.03	1.06	1.03	1.11	1.06
A | 30 km/h | profile	0.08	2.38	0.944	1.13	1.12	1.11	1.10	1.02	1.02	1.24	1.23	1.51	1.48	1.19	1.19
A | 50 km/h | profile	0.10	2.81	1.069	1.15	1.13	1.15	1.13	1.13	1.11	1.27	1.24	1.44	1.39	1.33	1.30
A | 70 km/h | profile	0.11	3.44	1.074	1.09	1.08	1.03	1.02	1.25	1.20	1.20	1.19	1.34	1.30	1.51	1.45
A | 100 km/h | profile	0.12	4.53	1.018	1.05	1.05	1.01	1.00	1.26	1.21	1.20	1.18	1.15	1.12	1.50	1.42
B | 30 km/h | profile	0.13	4.41	1.758	1.09	1.07	1.06	1.04	1.01	1.00	1.16	1.14	1.21	1.16	1.09	1.07
B | 50 km/h | profile	0.17	4.68	1.880	1.08	1.06	1.08	1.05	1.09	1.07	1.16	1.12	1.21	1.16	1.20	1.16
B | 70 km/h | profile	0.19	6.11	1.766	1.06	1.04	1.00	1.00	1.13	1.09	1.13	1.09	1.18	1.15	1.30	1.20
B | 100 km/h | profile	0.22	8.91	1.705	1.03	1.02	0.97	0.98	1.15	1.09	1.08	1.06	1.09	1.05	1.42	1.33
C | 30 km/h | profile	0.24	7.70	3.524	1.05	1.03	1.02	1.01	1.00	1.00	1.11	1.07	1.10	1.07	1.06	1.04
C | 50 km/h | profile	0.31	8.65	3.663	1.05	1.03	1.02	1.01	1.04	1.02	1.10	1.06	1.10	1.06	1.16	1.10
A | profile | none	0.10	2.58	3.808	1.12	1.11	1.07	1.06	0.94	0.97	1.88	2.12	1.58	1.83	2.04	2.16
B | profile | none	0.18	5.12	4.222	1.07	1.05	1.02	1.01	0.97	0.98	1.93	2.06	1.51	1.72	2.03	2.07
A | profile | steer.	0.10	4.59	3.946	1.12	1.11	1.07	1.06	0.94	0.97	1.92	2.16	1.55	1.51	2.10	2.24
B | profile | steer.	0.18	6.80	4.308	1.09	1.07	1.01	1.01	0.96	0.98	1.92	2.04	1.25	1.19	2.07	2.12

© Clemens Deubel, Johannes Meinck, Tobias Schramm, Günther Prokop

Appendix I: Composition of SA Force

FIGURE I.1 Composition of SA force during cornering maneuvers.



© Clemens Deubel, Johannes Meinck, Tobias Schramm, Günther Prokop

© 2027 Clemens Deubel, Johannes Meinck, Tobias Schramm, Günther Prokop. Published by SAE International. This Open Access article is published under the terms of the Creative Commons Attribution License (http://creativecommons.org/licenses/by/4.0/), which permits distribution, and reproduction in any medium, provided that the original author(s) and the source are credited.

Positions and opinions advanced in this work are those of the author(s) and not necessarily those of SAE International. Responsibility for the content of the work lies solely with the author(s).